Evolution of QPOs in GX 339–4 and EXO 1846–031 with Insight-HXMT and NICER

Zuobin Zhang, Honghui Liu, Divya Rawat, Cosimo Bambi, Ranjeev Misra, Pengju Wang, Long Ji, Shu Zhang, Shuangnan Zhang

The Astrophysical Journal, 971:148 (15pp), 2024 August 20 https://doi.org/10.3847/1538-4357/ad5a00

Evolution of QPOs in GX 339–4 and EXO 1846–031 with Insight-HXMT and NICER

Zuobin Zhang[1], Honghui Liu[1], Divya Rawat[2], Cosimo Bambi[1,3], Ranjeev Misra[4], Pengju Wang[5,6], Long Ji[7], Shu Zhang[5,6], and Shuangnan Zhang[5,6]
[1] Center for Astronomy and Astrophysics, Center for Field Theory and Particle Physics, and Department of Physics, Fudan University, Shanghai 200438, People's Republic of China; bambi@fudan.edu.cn
[2] Observatoire Astronomique de Strasbourg, Université de Strasbourg, CNRS, F-67000 Strasbourg, France
[3] School of Natural Sciences and Humanities, New Uzbekistan University, Tashkent 100007, Uzbekistan
[4] Inter-University Center for Astronomy and Astrophysics, Ganeshkhind, Pune 411007, India
[5] University of Chinese Academy of Sciences, Chinese Academy of Sciences, Beijing 100049, People's Republic of China
[6] Key Laboratory of Particle Astrophysics, Institute of High Energy Physics, Chinese Academy of Sciences, Beijing 100049, People's Republic of China
[7] School of Physics and Astronomy, Sun Yat-Sen University, Zhuhai 519082, People's Republic of China
Received 2023 May 30; revised 2024 June 6; accepted 2024 June 18; published 2024 August 14

Abstract

We conduct a spectral and timing analysis of GX 339−4 and EXO 1846−031 with the aim of studying the evolution of type-C quasiperiodic oscillations (QPOs) with spectral parameters. The high-cadence data from Insight-HXMT and NICER allow us to track the evolution of QPOs and spectra simultaneously. Type-C QPOs appear at the end of the low–hard state and/or the hard–intermediate state. Our results reveal that the QPO frequency is closely related to the inner disk radius and mass accretion rate in the two sources. This correlation aligns well with the dynamic frequency model of a truncated disk.

Unified Astronomy Thesaurus concepts: X-ray astronomy (1810); Low-mass x-ray binary stars (939); Astrophysical black holes (98); Stellar mass black holes (1611)

1. Introduction

Quasiperiodic oscillations (QPOs) refer to narrow peak structures in the power density spectrum (PDS), commonly observed in X-ray binaries (XRBs) (van der Klis 2005). In black hole systems, QPOs are mainly classified into low-frequency QPOs (LFQPOs, centroid frequency 0.1–30 Hz) and high-frequency QPOs (HFQPOs, centroid frequency $\geqslant$60 Hz) (Belloni 2010). Samimi et al. (1979) reported "sporadic quasiperiodic behavior" in the light curve of GX 339−4, and Motch et al. (1983) reported the first rigorous detection of QPOs for the same source. It was immediately recognized that QPOs could be a powerful tool to study the accretion process around black holes.

Over the last 40 years, especially after the launch of Rossi X-ray Timing Explorer, we have accumulated a lot of knowledge about QPOs. Using a broken power law to fit the broadband noise in the PDS, and a Lorentz function with a centroid frequency of $f_{\rm QPO}$ to fit the LFQPOs, Wijnands et al. (1999) found a significant positive correlation between the break frequency $f_{\rm b}$ and the frequency of the LFQPOs $f_{\rm QPO}$. Psaltis et al. (1999) reported a significant positive correlation between the frequency of LFQPOs and the frequency of the broadband noise (or HFQPOs) in low-mass XRBs (LMXBs), including black holes and neutron stars.

We have observed LFQPOs in most black hole XRBs and realized that LFQPOs can be divided into three types—A, B, and C—based on quality factor, noise type, fractional rms, and phase delay (e.g., Wijnands et al. 1999; Sobczak et al. 2000; Casella et al. 2005; Motta et al. 2011). Different types of QPOs occupy distinct regions on the hardness–intensity diagram, and are significantly distributed in different areas on the diagram of centroid frequency versus rms (e.g., Motta et al. 2011). The phenomenon of rapid transition between different types of QPOs has been found in some sources, and the timescale of this phenomenon can be very short (10 s; e.g., Bogensberger et al. 2020). In this work, we only focus on type-C QPOs.

Type-C QPOs appear in the early stage of the outburst, particularly at the hard–intermediate state and at the end of the low–hard state. The centroid frequency varies from a few mHz to ∼10 Hz, and is tightly correlated with the spectral state. Vignarca et al. (2003) reported a positive correlation between the centroid frequency and the photon index Γ. Motta et al. (2011) found the centroid frequency of type-C QPOs to significantly correlate with the coronal flux and disk flux. The dependence of the QPO frequency on photon energy was illustrated by Qu et al. (2010).

In addition to the phenomenological study of QPOs, many studies have been done on their theoretical explanation. Most theoretical models explain the QPO phenomenon through the following two different mechanisms: instabilities of the corona–disk system (e.g., Titarchuk & Fiorito 2004; Mastichiadis et al. 2022; Varnière et al. 2012) or the geometrical effects of general relativity (e.g., Stella & Vietri 1998; Ingram et al. 2009). Titarchuk & Fiorito (2004) introduced a transition layer in the corona–disk system to explain the QPO phenomenon in XRBs. The disk–corona natural frequency model was proposed by Mastichiadis et al. (2022), and they argued that type-C QPOs arise from the interaction of the hot corona with the cold accretion disk. Varnière et al. (2012) suggested that LFQPOs could result from the relativistic accretion–ejection instability.

Ingram et al. (2009) interpreted the QPOs in LMXBs as Lense–Thirring precession of the hot flow inside a truncated disk. Also in the frame of Lense–Thirring precession, Stella & Vietri (1998) proposed that LFQPOs are due to precession of the innermost region of the accretion disk. In recent years, more and more models and observational evidence have been

reported (e.g., Karpouzas et al. 2020; García et al. 2021; Bellavita et al. 2022; Méndez et al. 2022; Peirano et al. 2023). However, a unified model that can explain all QPO behavior has not been found yet.

Recently, Misra et al. (2020) identified the QPO frequency of GRS 1915+105 as the relativistic dynamic frequency of a truncated accretion disk with AstroSat observation data. The authors found a strong correlation between the QPO frequency divided by the accretion rate and the inner disk radius. The correlation is consistent with the prediction of the dynamic frequency model under the assumption of a standard relativistic accretion disk (Novikov & Thorne 1973). Liu et al. (2021a) extended the relation to cover a wider range of variations and confirmed the high-spin nature of the black hole in GRS 1915+105 with the data from Insight-HXMT (dubbed HXMT; Zhang et al. 2014). We note that GRS 1915+105 is a persistent source with particular properties (Belloni et al. 2000). We would like to test whether this relation holds for other sources that differ from GRS 1915+105, and we notice that there are two appropriate sources, GX 339−4 and EXO 1846−031, in the archive.

The XRB transient GX 339−4 is a typical LMXB discovered in 1973 (Markert et al. 1973). It undergoes a bright outburst every few years, and all four X-ray states typically seen in XRBs have been detected in this system (e.g., Miyamoto et al. 1995; Homan & Belloni 2005; Plant et al. 2014). GX 339−4 is located at 8–12 kpc and has a black hole mass of 4–11 $M_{\odot}$ (Zdziarski et al. 2019). Strong relativistic reflection signatures have been found in this source in both the hard and soft states (e.g., Miller et al. 2004; García et al. 2015; Liu et al. 2022, 2023). Previous studies have indicated that the black hole in GX 339−4 has a very high spin ($a_{*} \sim 0.95$, García et al. 2015; Parker et al. 2016). The inclination angle of the accretion disk should have an intermediate value (Fürst et al. 2015; Parker et al. 2016). Motta et al. (2011) systematically studied the properties of QPOs of GX 339−4 and suggested that the centroid frequency of QPOs (including type-C QPOs) correlates with the disk flux.

EXO 1846−031 was discovered by the European X-ray Observatory Satellite (EXOSAT) when it went into outburst in 1985 April, and then it was considered an LMXB (Parmar et al. 1993; Draghis et al. 2020). CGRO/BATSE detected a second outburst in 1994 (Zhang et al. 1994). Subsequently, the source remained in a quiescent state for 25 years. In 2019, EXO 1846−031 experienced a new outburst, monitored by X-ray missions (e.g., MAXI/GSC, HXMT, NuSTAR) and radio telescopes (e.g., MeerKAT, AMI-LA). A high-quality observation was conducted by NuSTAR on 2019 August 3, with a 22.2 ks exposure time. Draghis et al. (2020) reported strong relativistic reflection features with the sensitive NuSTAR spectra, concluding that the source is a black hole with a nearly maximal spin parameter ($a_{*} = 0.997$) at a disk inclination of $\theta = 73°$. EXO 1846−031 is located at 2.4–7.5 kpc, according to the previous studies on X-ray and radio data (Parmar et al. 1993; Williams et al. 2022), and has a black hole mass of $\sim 9\ M_{\odot}$ (Draghis et al. 2020; Williams et al. 2022). Liu et al. (2021b) reported the observational results from a detailed timing analysis of the 2019 outburst of EXO 1846−031 using the data from HXMT and NICER.

In this work, we focus on the latest HXMT and NICER observations of GX 339−4 and EXO 1846−031, and present a detailed temporal and spectral analysis. The paper is organized as follows. Section 2 presents the observational data reduction. The spectral timing analysis is reported in Section 3. We discuss the results and report our conclusions in Sections 4 and 5, respectively.

2. Observations and Data Reduction

2.1. Data Selection

Starting in 2021 February, GX 339−4 went into a new outburst that lasted for a few months. Figure 1 shows the long-term light curve in the 2–20 keV band and the corresponding hardness observed with MAXI/GSC. The hardness is defined as the ratio between the count rates at 4–10 keV and 2–4 keV. Both HXMT and NICER extensively observed the 2021 outburst of the source. We went through all available HXMT and NICER data and picked out those observations that show type-C QPO signatures. Type-C QPOs are characterized by the narrow peak and its harmonic in the PDS, together with a strong flat-top broadband noise. The selected observations analyzed in this work are marked in the light curve of GX 339−4 in Figure 1. Information about these observations is listed in Table A1 in the Appendix.

The 2019 outburst of EXO 1846−031 was first detected by MAXI/GSC on 2019 July 23 (Negoro et al. 2019), and it lasted about 3 months. The long-term MAXI light curve and the corresponding hardness are shown in Figure 2. Just as for GX 339−4, both HXMT and NICER conducted high-cadence pointing observations of EXO 1846−031. Type-C QPOs appear during the transition from hard to soft state (Liu et al. 2021a). We selected observations showing type-C QPO signatures. The selected observations are marked in the light curve in Figure 2 and listed in Table A2.

We show the hardness–intensity diagrams of GX 339−4 and EXO 1846−031 in Figures 3 and 4, respectively. The red diamonds represent the HXMT and NICER observations that show type-C QPO features.

2.2. Data Reduction

HXMT covers the broadband energy range 1–250 keV with low-energy (LE), medium-energy (ME), and high-energy (HE) detectors (Cao et al. 2020; Chen et al. 2020; Liu et al. 2020; Zhang et al. 2020). The light curves and spectra are extracted using the HXMT data analysis software (HXMTDAS) version 2.05 and CALDB version 2.06, following the official user guide. The background is estimated by the standalone scripts `hebkgmap`, `mebkgmap`, and `lebkgmap` (Guo et al. 2020; Liao et al. 2020a, 2020b). The data are screened following the recommended criteria, i.e., an elevation angle $>10°$, a geomagnetic cutoff rigidity >10 GeV, a pointing offset angle $<0.1°$, and at least 300 s away from the South Atlantic Anomaly (SAA).

The NICER data are processed with the NICER data analysis software (NICERDAS) version 2021-04-01_V008 and CALDB version 20210707. We apply standard filtering criteria: the pointing offset is less than 54″, and the pointing direction is more than 40° away from the bright Earth limb, more than 30° away from the dark Earth limb, and outside the SAA. Additionally, we exclude data from detectors #14 and #34, which are affected by episodes of increased electronic noise. We select events not flagged as "overshoot" or "undershoot" resets (EVENT_FLAGS = bxxxx00) or forced triggers (EVENT_FLAGS = bx1x000). The standard NICER

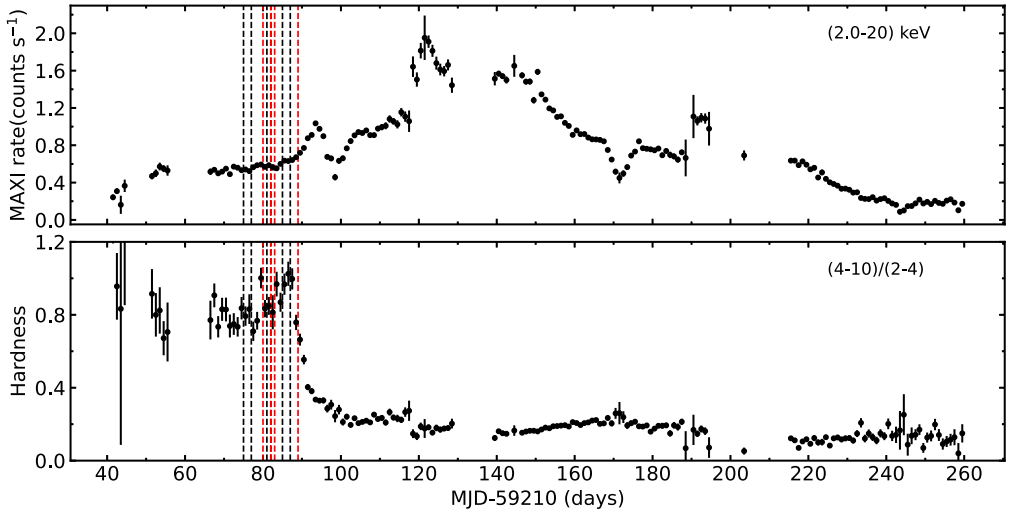

Figure 1. MAXI/GSC light curve and corresponding hardness of GX 339−4 starting from 2021 February 5 (MJD = 59250). The hardness is defined as the ratio between the count rates in the 4–10 keV and 2–4 keV bands. The vertical black lines mark the HXMT observations analyzed in this work and the vertical red lines mark the NICER observations.

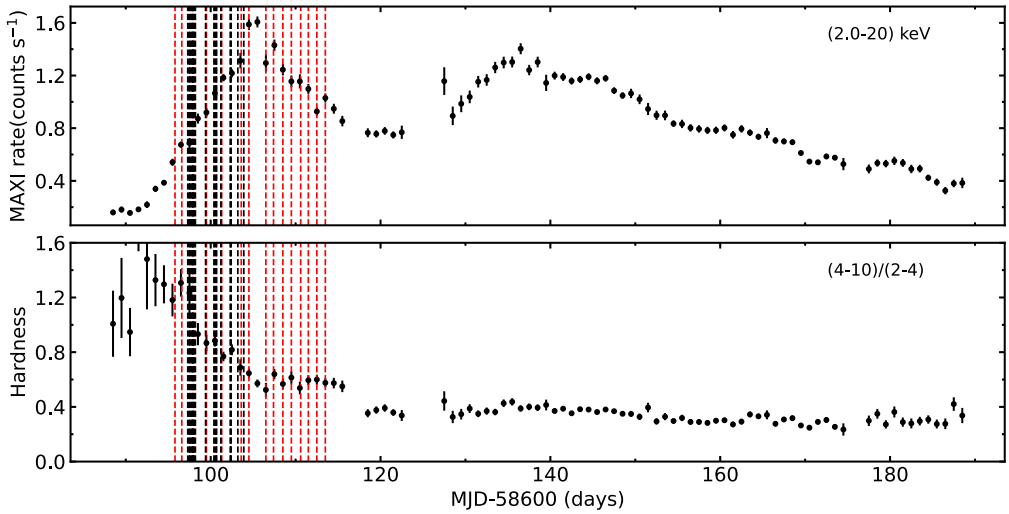

Figure 2. MAXI/GSC light curve and corresponding hardness of EXO 1846−031 starting from 2019 June 16 (MJD = 58650). The hardness is defined as the ratio between the count rates in the 4–10 keV and 2–4 keV bands. The vertical black lines mark the HXMT observations analyzed in this work and the vertical red lines mark the NICER observations.

reduction routine `nicerl2` is used to process the data. The cleaned events are barycenter-corrected using the FTOOL `barycorr`. We extract the energy spectra of the background in each observation using the `nibackgen3C50` tool (Remillard et al. 2022). The redistribution matrix file and ancillary response file are created by using the tasks `nicerrmf` and `nicerarf`, respectively.

3. Data Analysis

3.1. Timing Analysis

We extract HXMT LE and NICER X-ray timing instrument (XTI) light curves with a time resolution of 1 ms from the full energy band (1–10 keV in HXMT; 0.5–10 keV in NICER) for each HXMT observation and NICER observation. In order to calculate hardness ratios, we also produce LE light curves from the 1–5 keV and 5–10 keV bands, and XTI light curves from the 0.5–4 keV and 4–10 keV bands.

We carefully check the extracted light curves from all observations of GX 339−4 and find there are two NICER observations (Obs ID: 4133010103, 4133010104) that show relatively strong variability in count rate and hardness. Figure 5 shows the light curves of these two NICER observations. The gaps in the light curves are due to the low Earth orbit of the telescope or the SAA. We can clearly see that the source went through a period of increasing luminosity and decreasing hardness. Comparing with the location of these two observations in Figure 1 (the last red dotted line; in fact, since the two lines are quite close, they look like one line), we conclude that these two observations are during the hard-to-soft transition with the hardness continuously decreasing. Then we divide the observations according to the light curve, counting each snapshot as a sub-observation. After checking all sub-observation data, we select those with exposures longer than 200 s. The selected sub-observations are numbered 4133010103-1 through 4133010103-9, and 4133010104-1 through 4133010104-13, as shown in Figure 5. The other light

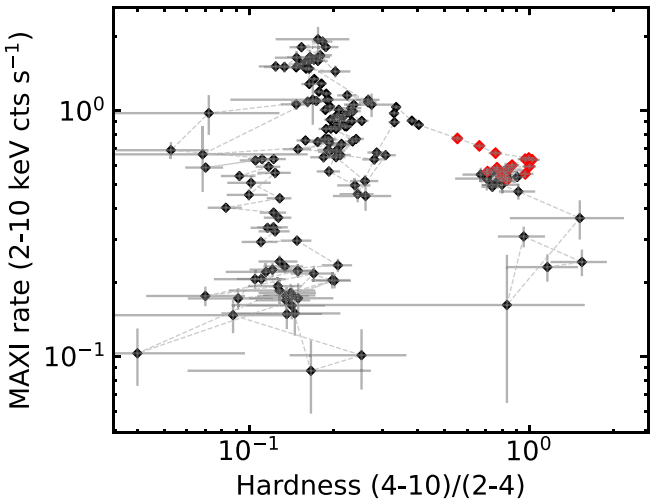

Figure 3. Hardness–intensity diagram of GX 339−4 with MAXI/GSC daily average data. The red diamonds represent the HXMT and NICER observations that show type-C QPOs.

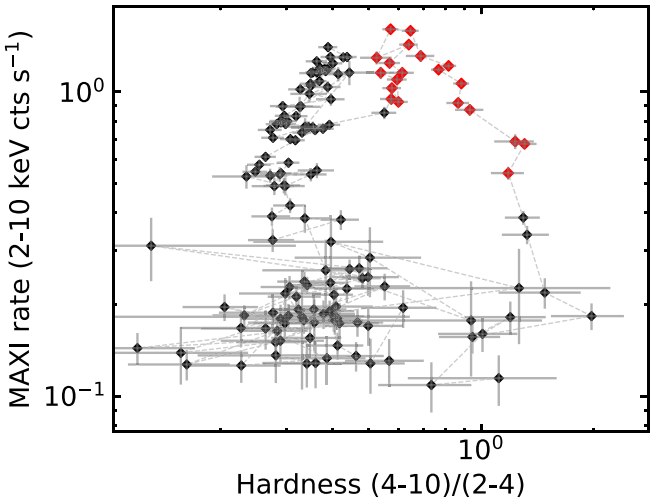

Figure 4. Hardness–intensity diagram of EXO 1846−031 with MAXI/GSC daily average data. The red diamonds represent the HXMT and NICER observations that show type-C QPOs.

curves do not show strong variability in the count rate, i.e., no distinctive evidence of flares, dips, or state transitions, ensuring a safe basis for timing and spectral analysis to characterize the source properties.

For EXO 1846−031, the count rate of the source remains fairly stable during each HXMT and NICER interval, and the hardness does not change dramatically. Therefore, we carry out timing and spectral analysis in the unit of one observation in this work.

To measure the QPO frequency ($f_{\rm QPO}$) of GX 339−4 and EXO 1846−031, we employ the `Python` package `Stingray` (Huppenkothen et al. 2019) to create a PDS for each observation. The light curves of both HXMT and NICER are split into 64 s segments, and then PDSs from all 64 s segments are averaged. The PDS is normalized according to the "rms" method (Belloni & Hasinger 1990), and logarithmically rebinned so that each bin size is 1.02 times larger than the previous bin. Note that we focus on the HXMT LE 1–10 keV light curve and the NICER XTI 0.5–10 keV light curve to extract the PDS and search for a QPO signal. The time resolution of both HXMT LE and NICER XTI light curves is 1 ms, corresponding to the Nyquist frequency of 500 Hz. The 8–30 keV HXMT ME light curves have been analyzed in the same way and return consistent measurements of the QPO frequencies. So we report only the results from LE data in this work.

We use XSPEC v12.12.1 (Arnaud 1996) to analyze the PDS. The typical PDS of XRBs manifests broad components and one or two narrow peaks at different frequencies, corresponding to broadband noise and the possible QPO fundamental and harmonics, respectively. We need at least one narrow Lorentzian for the QPO to fit the Poisson-extracted PDS (Belloni et al. 2002). More narrow Lorentzians are sometimes included to model harmonic peaks. All QPOs we detect have a quality factor (Q) greater than 4 and detection significance greater than 3σ, i.e., the ratio of the Lorentzian norm divided by its 1σ negative error is larger than 3. Figures A1 and A2 show a typical PDS and the fit results with several Lorentzian models for GX 339−4. Figures A3 and A4 show their counterparts for EXO 1846−031. The QPO frequencies for each observation are listed in Table A3 for GX 339−4 and Table A4 for EXO 1846−031.

3.2. Spectral Analysis

For spectral analysis of the HXMT data, we consider the LE data in the 2–10 keV band and ME data in the 8–20 keV band. ME data above 20 keV and HE data are ignored because of the very high background. Note that we ignore the data below 2 keV of the LE instrument in spectral analysis (instead of the 1 keV for timing analysis) because of calibration uncertainties in the low-energy band. For NICER data, we consider the 1–10 keV band in this section, ignoring the data below 1 keV because of calibration issues.

The HXMT and NICER spectra are fitted with the XSPEC (v12.12.1) package. The χ^2 statistics is employed and all parameter uncertainties are estimated at 90% confidence level, corresponding to $\Delta\chi^2 = 2.71$. All spectra are grouped to ensure minimum counts of 20 per bin. A systematic error of 1% is added to the NICER spectra.

The HXMT and NICER spectra of GX 339−4 are fitted with the model combination `Tbabs × (simpl × kerrd + relxill)`. `Tbabs` is included to account for absorption by the interstellar medium. The recommended photoelectric cross sections of Verner et al. (1996) and element abundances of Wilms et al. (2000) are used for the `Tbabs` component. We set its column density ($n_{\rm H}$) to be a free parameter for NICER spectra. With HXMT spectra, we cannot constrain $n_{\rm H}$ well, so we fix it at its best-fit value, 0.55×10^{22} cm^{-2}, which is consistent with the result of the NICER data and the value in the literature (e.g., Wang et al. 2020; Liu et al. 2022). `kerrd` accounts for the thermal emission from the geometrically thin and optically thick accretion disk (Ebisawa et al. 2003), in which the distance and mass of the black hole and the inclination angle of the accretion disk are set to 8.4 kpc, 9.0 $M_\odot$, and 30° (Parker et al. 2016), respectively. The spectral hardening factor of `kerrd` is set to 1.7 (Shimura & Takahara 1995). `simpl` (Steiner et al. 2009) is used to take into account for the Comptonization of disk photons by the corona. The source has been found to have strong reflection features (Liu et al. 2022), therefore we use the full reflection model `relxill` (García et al. 2014) to fit them. The spin

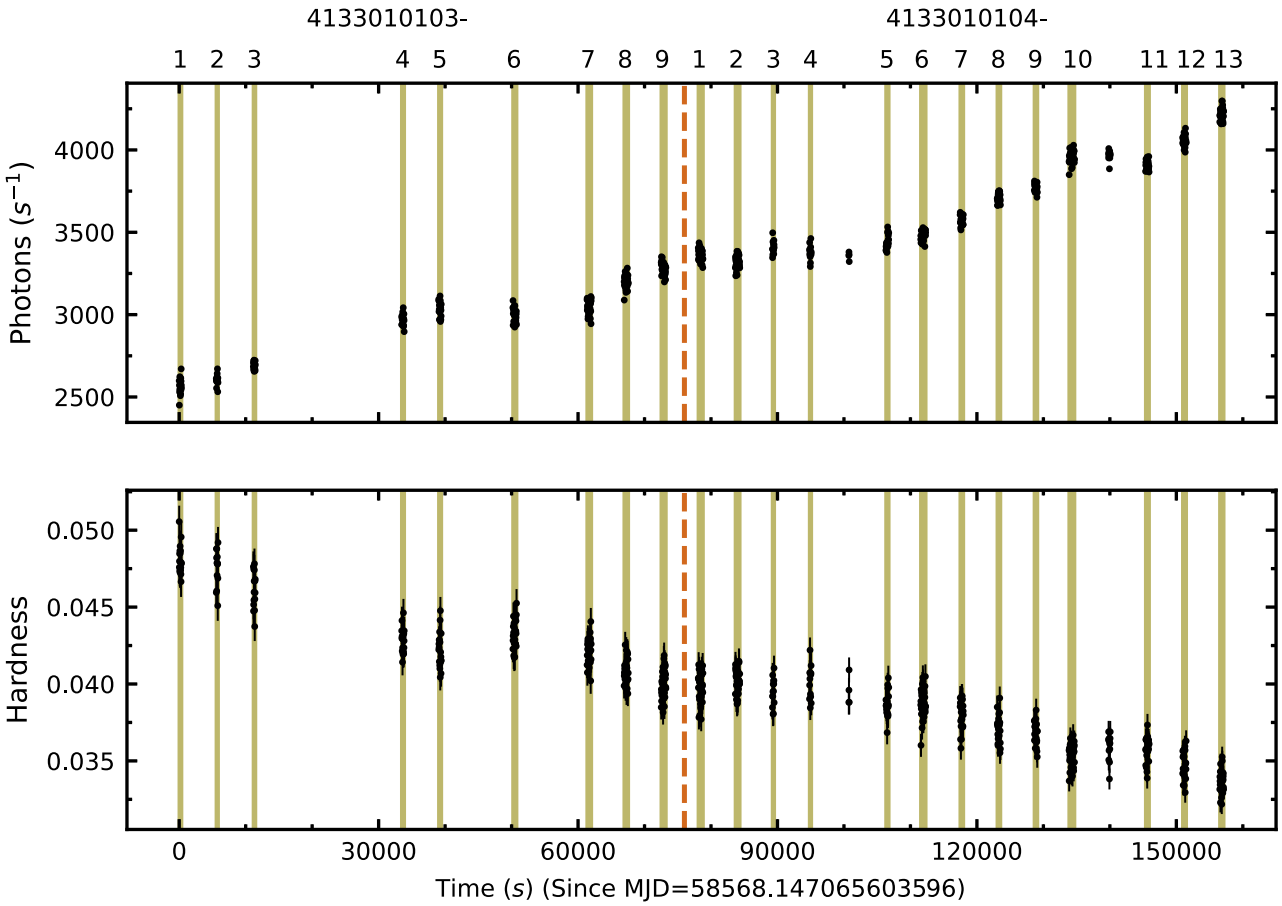

Figure 5. Light curves of GX 339−4 by NICER in the 0.5–10 keV band (top panel) and corresponding hardness (bottom panel) (Obs ID: 4133010103, 4133010104). The hardness is defined as the ratio between the count rates in the 4–10 keV and 0.5–4 keV bands. The source shows increasing flux and decreasing hardness during this period. The intervals with exposure >200 s are marked with yellow shading. The selected sub-observations are numbered 4133010103-1 through 4133010103-9, and 4133010104-1 through 4133010104-13.

parameter (a_*) is fixed at 0.95 (Parker et al. 2016). The index of the emissivity profile is fixed at 3 because it cannot be constrained by the fit. The iron abundance ($A_{\rm Fe}$) and reflection fraction are fixed at 1 and −1, respectively. The best-fit values and uncertainties are shown in Table A3. Figures A1 and A2 show typical spectra and fit results of HXMT data and NICER data, respectively.

In the case of EXO 1846−031, for HXMT spectra, the best-fit model is `Tbabs × (simpl × kerrd + relxill)`. The distance and mass of the black hole and the inclination angle of the accretion disk are set to 4.5 kpc (Williams et al. 2022), 10.0 $M_\odot$ (Draghis et al. 2020; Williams et al. 2022), and 73° (Draghis et al. 2020), respectively. The spin a_* is fixed at 0.998 (Draghis et al. 2020). We use a simple power law to model the emissivity profile ($q_{\rm in} = q_{\rm out}$). The other parameters are set exactly as in the case of GX 339−4. For NICER spectra, we notice that there are still some large residuals in the soft X-ray band with the same model, including a Gaussian-like emission near 1.1 keV and edge-like shapes near 1.8 keV. These energies correspond to features in the effective area of NICER versus energy (e.g., Wang et al. 2020), where those at 1.1 and 1.8 keV are attributed to sodium and silicon, respectively. Therefore, we adopt the following model for the NICER spectra: `Tbabs × (simpl × kerrd + relxill + Gaussian) ×edge`. This calibration issue arises in EXO 1846−031 because the source has high interstellar absorption, which makes the photon count rate in the lower energy band relatively low and thus makes the calibration issue prominent. Typical spectra and fit results of HXMT and NICER are shown in Figures A3 and A4. In Table A4, we summarize the best-fit values and errors of EXO 1846−031.

4. Results and Discussion

Figures 6 and 7 show the evolution of inner radius ($R_{\rm in}$) and $f_{\rm QPO}$ with time for GX 339−4 and EXO 1846−031, respectively. Generally speaking, we clearly see that the value of $f_{\rm QPO}$ monotonically increases with time. The behavior is consistent with that reported in Motta et al. (2011) and Liu et al. (2021b). It has also been observed in other XRBs, for example, XTE J1859+226 (Casella et al. 2004). In addition, a notable feature for both sources is the decrease of $R_{\rm in}$. For GX 339−4, the inner disk moves toward the innermost stable circular orbit, from $>50R_{\rm g}$ to $\sim 7R_{\rm g}$ ($R_{\rm g}$ is the gravitational radius), which coincides with the result of previous study (e.g., Wang-Ji et al. 2018; Wang et al. 2020). Although there are some variable features, EXO 1846−031 shows a similar trend. The left panels of Figures 6 and 7 show a break in the relation for GX 339−4 and EXO 1846−031, respectively. The same is true for the QPO frequency in the right panels. This break in the relation is most likely related to the transition from hard state to hard–intermediate state, as suggested by Wang et al. (2022).

Correlation between the parameters involved in temporal and spectral analysis is shown in Figures 8 and 9. An interesting

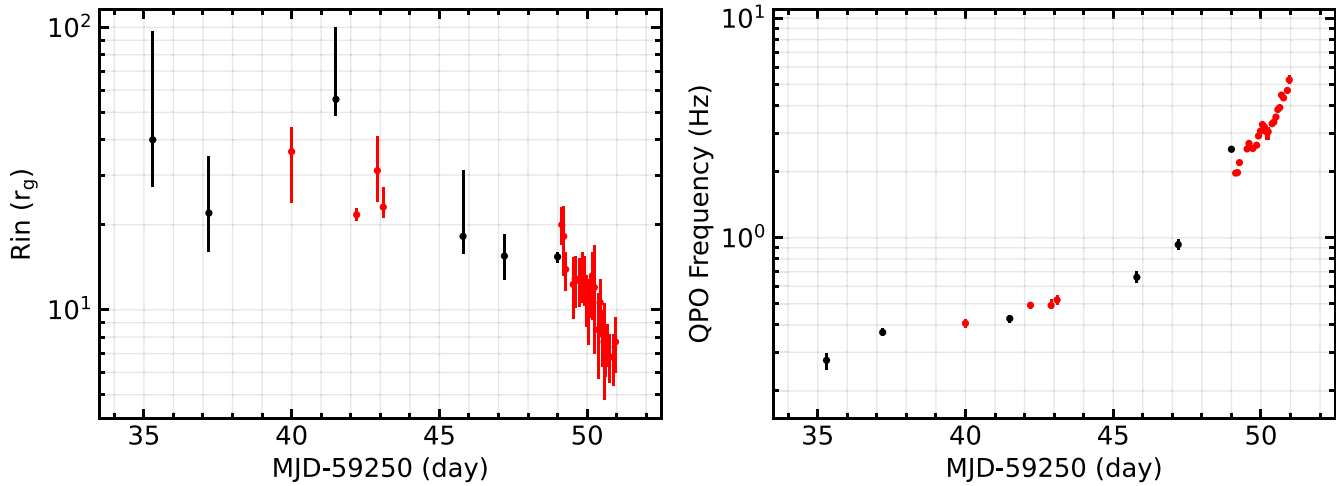

Figure 6. Evolution of disk inner radius R_{in} (left panel) and QPO frequency (f_{QPO}) with MJD in GX 339−4. The black points indicate HXMT data and the red dots indicate NICER data.

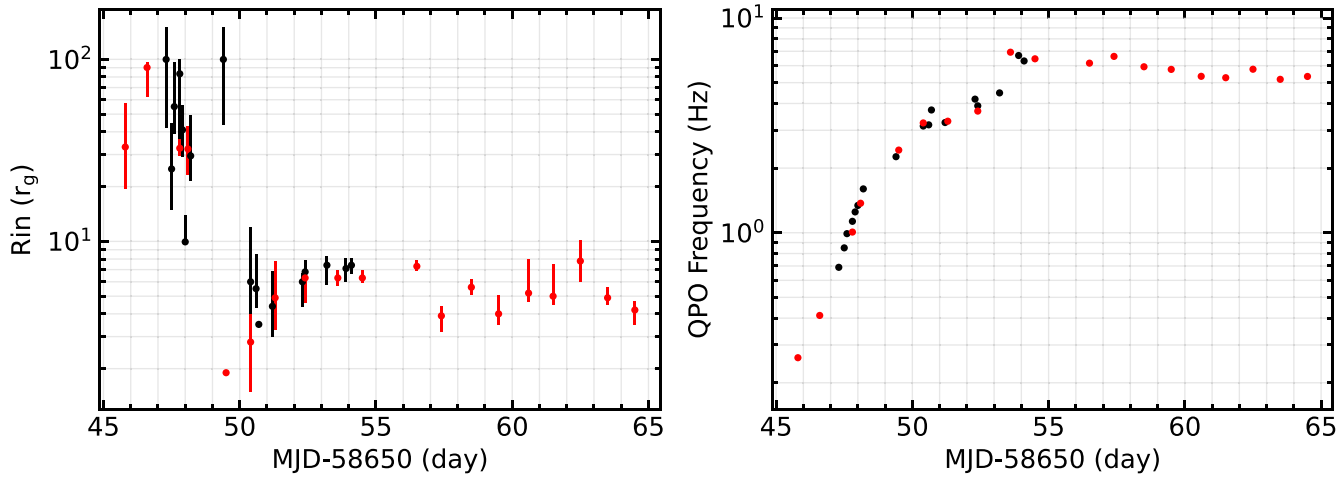

Figure 7. Evolution of disk inner radius R_{in} (left panel) and QPO frequency (f_{QPO}) with MJD in EXO 1846−031. The black points and red points represent the results of HXMT data and NICER data, respectively.

result is the relationship between the photon index (Γ) and f_{QPO}. The results from both sources exhibit the same tendency, as shown in the bottom panels of Figures 8 and 9. There is a significant positive correlation between Γ and f_{QPO} initially, which flattens or starts reversing at the highest values of f_{QPO}. The turnoff in the correlation is not apparent in GX 339−4, while it is evident in EXO 1846−031 (around $\Gamma \sim 2.7$). Similar correlations have been reported in a number of other LMXBs (e.g., Vignarca et al. 2003; Titarchuk & Fiorito 2004; Titarchuk & Seifina 2009; Fürst et al. 2016). Titarchuk & Fiorito (2004) introduced the transition layer (TL) model to explain the observed correlations. The TL model depicts how the QPOs are related to the coronal properties (e.g., the size, optical depth, temperature, and spectral index) and predicts the correlation between photon index and QPO frequency. The results we get are in significant agreement with the predictions of the model, except for the observations of EXO 1846−031 with $f_{QPO} > 5.18$ Hz, where a negative correlation between f_{QPO} and Γ appears. A universal explanation of this correlation between Γ and f_{QPO} is still missing.

The upper left panel of Figure 8 shows a broad anticorrelation between f_{QPO} and R_{in} in GX 339−4. This anticorrelation is not particularly significant in EXO 1846−031, and we can only observe a general tendency of larger R_{in} corresponding to a smaller frequency, as shown in the upper left panel of Figure 9. The same correlation between the QPO frequency and the disk inner radius was reported in other sources (e.g., GRS 1915+105; Rodriguez et al. 2002). The hot flow Lense–Thirring precession model would predict anticorrelation between f_{QPO} and R_{in} (Ingram et al. 2009; Ingram & Done 2010). To check the possibility of modeling the results with the relativistic precession model, we plot the precession frequency calculated with Equation (2) of Ingram et al. (2009), assuming $a_* = 0.3$, 0.5, 0.7, 0.9, and 0.998. In these calculations, we choose $\zeta = 0$ and the inner radius of hot flow $r_i = 3.0(h/r)^{-4/5}a_*^{2/5}$ (with $h/r = 0.2$), following Ingram et al. (2009). We see the model cannot explain the results we obtained, either for GX 339−4 or for EXO 1846−031, as shown in the plot.

The variation of the QPO frequency with the accretion rate ($\dot{M}$) is shown in the upper right panels of Figures 8 and 9. Liu et al. (2021a) reported a strong correlation between the QPO frequency and mass accretion rate in GRS 1915+105 with HXMT data. We do not find any significant correlation

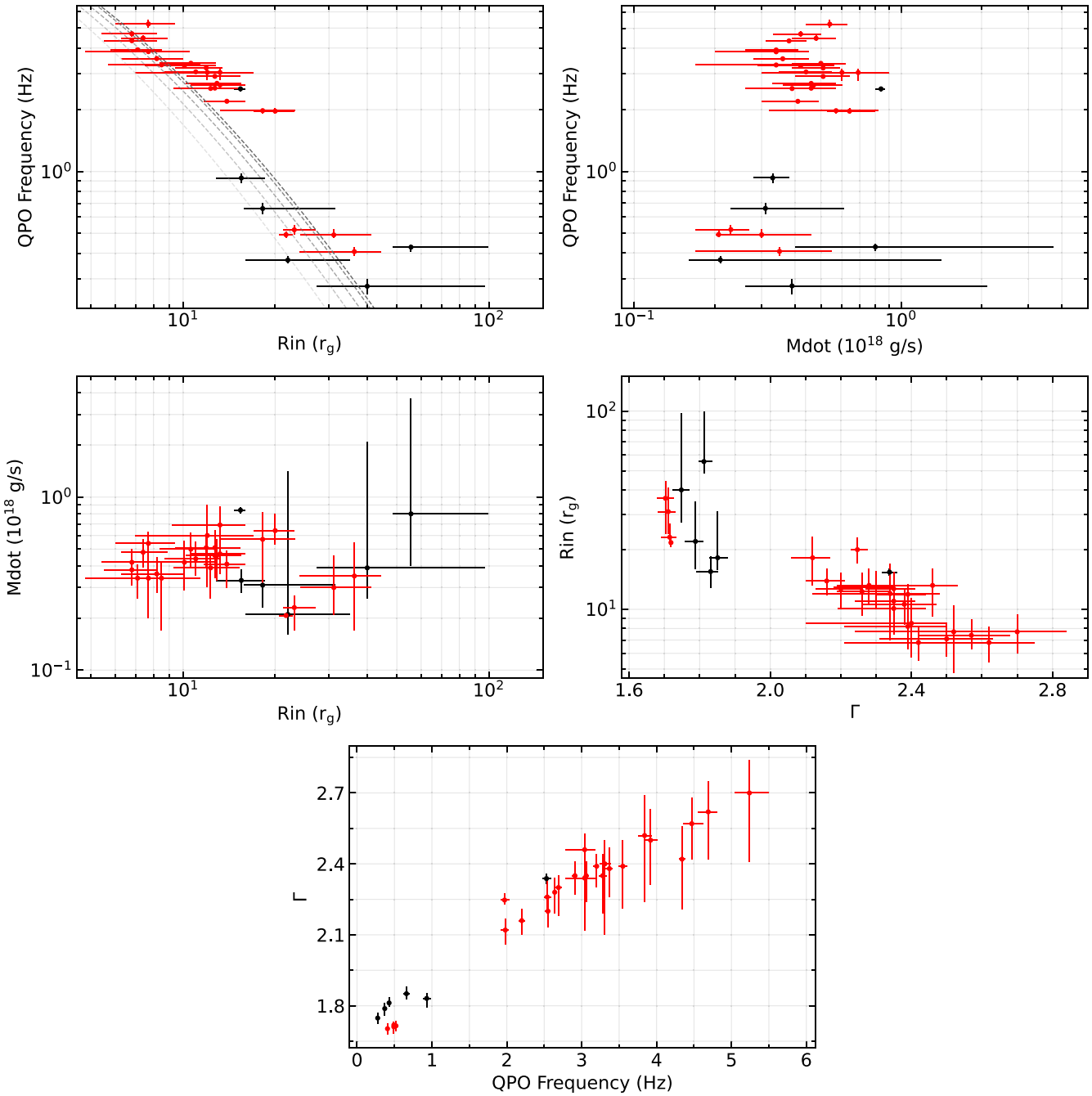

Figure 8. Correlation between the parameters involved in the temporal and spectral analysis in the case of GX 339−4. Correlations of the QPO frequency vs. inner disk radius and the QPO frequency vs. accretion rate are shown in the upper left and upper right panels. The two central panels illustrate the accretion rate vs. inner disk radius and inner disk radius vs. photon index. The photon index vs. QPO frequency is depicted in the bottom panel. The black and red crosses denote the results of HXMT data and NICER data, respectively. In the top left panel, the dashed gray lines represent the correlation of the frequency and inner radius predicted by the Lense–Thirring precession model. The lines from left to right depict $a_* = 0.3$, 0.5, 0.7, 0.9, and 0.998.

between them in GX 339−4, while there is a weak anticorrelation in EXO 1846−031. In fact, a positive correlation between $f_{\rm QPO}$ and $\dot{M}$ is proposed in the TL model by Titarchuk & Fiorito (2004), and in the disk–corona natural frequency model by Mastichiadis et al. (2022). Figure 3 of Titarchuk & Fiorito (2004) depicts the positive correlation between $f_{\rm QPO}$ and the γ-parameter (which is proportional to mass accretion rate), which is opposite to what we find. Mastichiadis et al. (2022) argued that type-C QPOs could arise from the interaction of the hot corona with the cold accretion disk, and they predict a formula $f_0 \propto \dot{M}^{1/2}$, for a certain radius of the corona and ratio of hard to soft radiation (Figure 5 of Mastichiadis et al. 2022). This model possibly reproduces the relation between $f_{\rm QPO}$ and $\dot{M}$ of our cases, allowing for continuous variations of parameters, such as the size of corona and corona–disk radiative feedback. Our spectral fits do not provide information on these parameters. So we do not explore such a possibility further.

Misra et al. (2020) identified QPOs as the dynamic frequency of a truncated relativistic accretion disk in the case

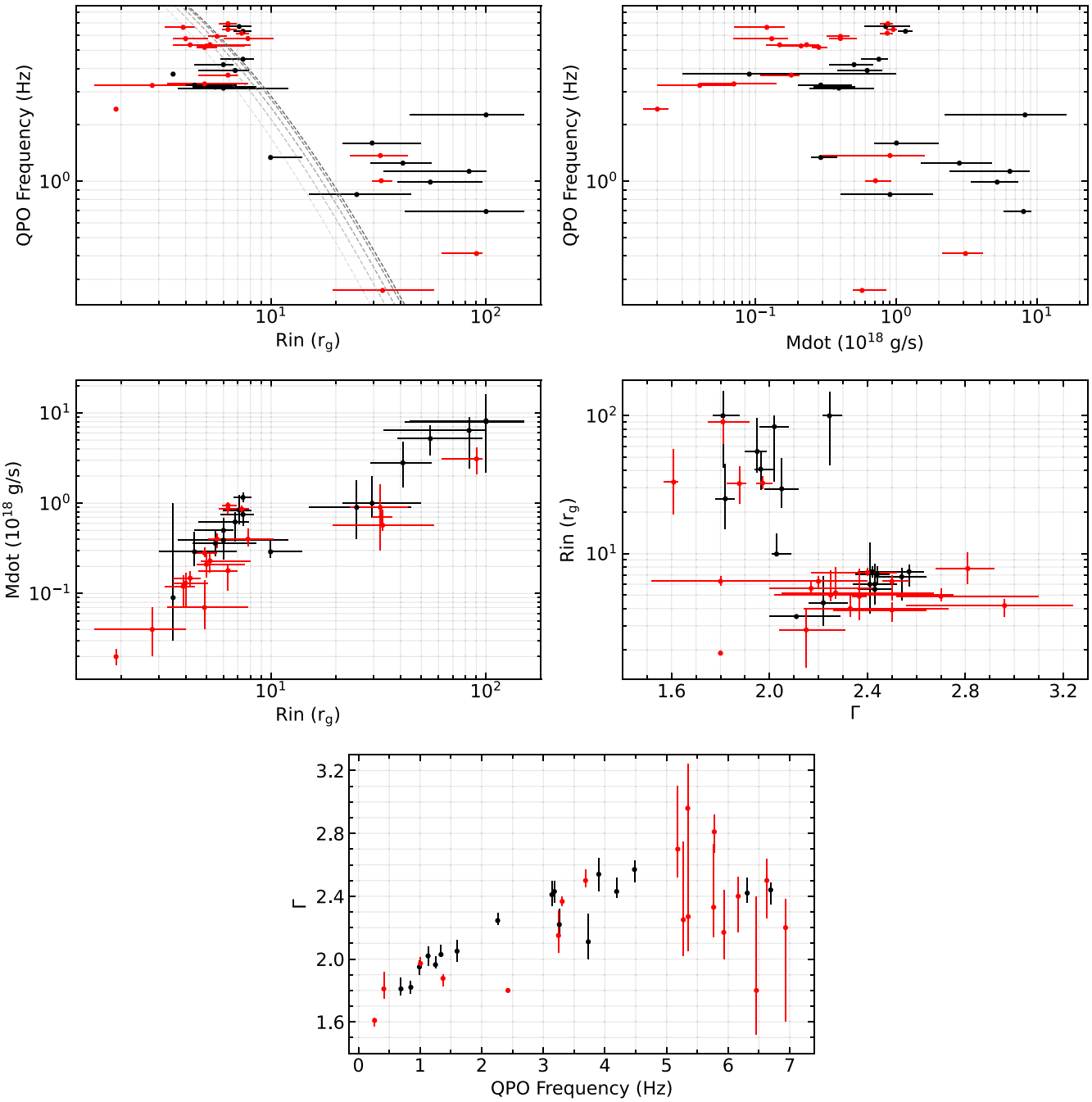

Figure 9. Correlation between the parameters involved in temporal and spectral analysis in the case of EXO 1846−031. The figure is organized in the same way as Figure 8.

of GRS 1915+105. The dynamic frequency is defined as the ratio of the sound propagation velocity of the inner disk to the truncation radius, i.e., the inverse of the sound crossing time (Misra et al. 2020). Based on the assumption that the accretion disk is a standard relativistic accretion disk (Novikov & Thorne 1973), the dynamic frequency is a function of $R_{\rm in}$, a_*, $\dot{M}$, and a normalization factor (N). Liu et al. (2021a) extended the results of Misra et al. (2020) to a larger range of accretion rates with HXMT data of GRS 1915+105, and confirmed the high-spin nature of the source. Following the work of Misra et al. (2020) and Liu et al. (2021a), we illustrate the relation between $f_{\rm QPO}$ divided by $\dot{M}$ and $R_{\rm in}$ in Figures 10 and 11. Both sources show negative correlation between $f_{\rm QPO}/\dot{M}$ and $R_{\rm in}$. Moreover, the correlation follows the prediction of the dynamic frequency model.

We fit the relation between $f_{\rm QPO}/\dot{M}$ and $R_{\rm in}$ using Equation (3) in Misra et al. (2020). We calculate χ^2 as

$$\chi^2 = \sum_{n=1}^{N} \frac{(y_i - f(x_i))^2}{\delta_i^2}$$

where $\delta_i^2 = (\partial f/\partial x)^2(\delta x_i)^2 + (\delta y_i)^2$, and δx_i and δy_i are the errors of x_i and y_i, respectively. The fit returns $a_* = 0.9978 \pm 0.0009$ and $N = 0.281 \pm 0.025$ for EXO 1846−031, indicating a rapidly spinning black hole. This result is consistent with what has been reported by analyzing the blurred

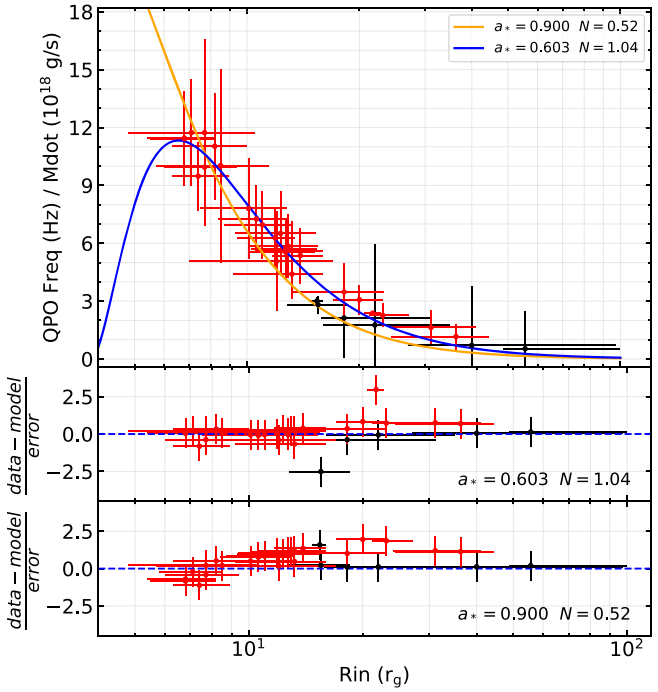

Figure 10. Top: variation of QPO frequency divided by the accretion rate vs. inner disk radius in the case of GX 339−4. The results of HXMT data and NICER data are denoted with black and red crosses, respectively. The orange curve represents the best fit ($a_* = 0.603$, $N = 1.02$), and the blue curve corresponds to $a_* = 0.900$, $N = 0.52$. Middle: residuals of the model ($a_* = 0.603$, $N = 1.02$) to data. Bottom: residuals of the model ($a_* = 0.900$, $N = 0.52$) to data. In the middle and bottom panels, the y-axes are scaled for clarity and there are, respectively, one and two points that are outside the plots.

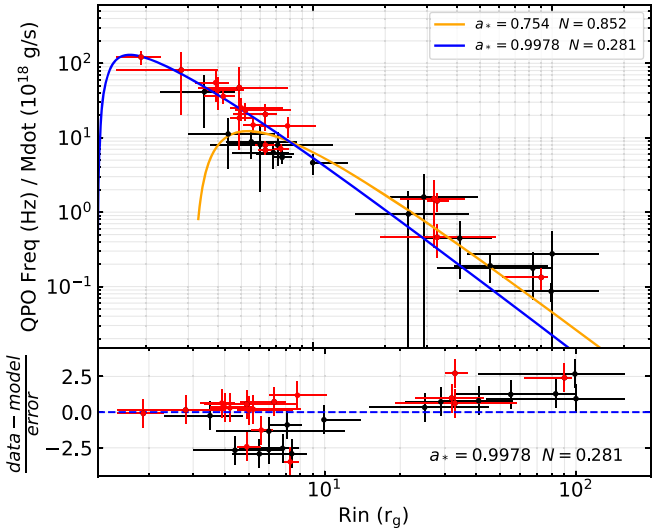

Figure 11. Top: variation of QPO frequency divided by the accretion rate vs. inner disk radius in the case of EXO 1846−031. The black and red crosses denote the results of HXMT data and NICER data, respectively. The blue curve shows the best fit. The orange curve represents the best fit ($a_* = 0.754$, $N = 0.853$) when we only include the data with $R_{\rm in} > 5R_{\rm g}$. This proves that the data with small $R_{\rm in}$ are important to fit the spin parameter. Bottom: residuals of the best-fit model ($a_* = 0.9978$, $N = 0.281$) to data. The y-axis is scaled for clarity and there are three points that are outside the plots.

reflection spectra (e.g., Draghis et al. 2020; Abdikamalov et al. 2021). The best-fit curve is shown in Figure 11. Note that in the plots for residuals, we only consider the contribution of the error of the y-axis.

In the case of GX 339−4, the fit returns $a_* = 0.603 \pm 0.026$ and $N = 1.02 \pm 0.05$. Such a low-spin result is somewhat different from the result obtained by analyzing the blurred reflection spectra or thermal spectra (e.g., Reis et al. 2008; García et al. 2015; Ludlam et al. 2015; Parker et al. 2016; Wang et al. 2020). We note that for this source we do not have data below $6R_{\rm g}$. The relativistic effects are more evident at lower $R_{\rm in}$ ($3R_{\rm g} \sim 5R_{\rm g}$). Hence, data points at lower $R_{\rm g}$ play a crucial role in the estimation of the spin parameter. In Figure 10, we simultaneously show two curves, $a_* = 0.603$ and $a_* = 0.900$. It is worth noting that the most important difference between the two curves is reflected in the region with low $R_{\rm in}$. This also proves our view that a reasonable fitting value cannot be obtained because of the lack of data with relatively small $R_{\rm in}$.

The evolution of QPO frequency is generally consistent with the prediction of the dynamic frequency model. However, the residuals still show a trend: negative values always appear at low $R_{\rm in}$ while positive values appear at large $R_{\rm in}$. We note that the dynamic frequency model is a very simple assumption. It might not be able to capture all of the factors that drive the variability of the LFQPOs. Therefore it is reasonable that we find some differences between different observations.

The middle right panels of Figures 8 and 9 show that the inner disk radius tends to decrease when Γ increases. This behavior is consistent with that expected during a hard-to-soft transition. A noteworthy positive correlation between $\dot{M}$ and R_{in} in EXO 1846−031 is described in the middle left panel of Figure 9. A similar relationship was reported in GRS 1915 +105 (Misra et al. 2020; Liu et al. 2021a; Rawat et al. 2022) and in MAXI J1535-571 (Garg et al. 2022). This correlation does not follow the expected behavior of the truncated disk model (Done et al. 2007). But Dullemond & Spruit (2005) predicted a positive correlation between $\dot{M}$ and $R_{\rm in}$ (see their Figure 8), calculating the evaporation of the cool accretion disk on account of the ion bombardment. An alternative explanation is discussed in Abramowicz et al. (1978), where the authors suggested a larger inner edge is required when the mass accretion rate increases to dissipate the angular momentum of accretion material. For these models, a detailed study is beyond the scope of this work, and we leave it for future work.

5. Conclusion

We investigate the temporal and spectral properties from the latest HXMT and NICER observing campaign of GX 339−4 and EXO 1846−031. Temporal and spectral analyses show that the evolution of the QPO frequency is closely related to mass accretion rate and inner disk radius in both sources, and is generally consistent with the prediction of the dynamic frequency model. We extend the application of the model from GRS 1915+105, a persistent source, to these two transient sources, and confirm the high-spin nature of the black hole in EXO 1846−031.

Acknowledgments

This work was supported by the National Natural Science Foundation of China (NSFC), grant No. 12250610185, 11973019, and 12261131497, the Natural Science Foundation of Shanghai, grant No. 22ZR1403400, and the Shanghai Municipal Education Commission, grant No. 2019-01-07-00-07-E00035.

Appendix

The left panels in Figures A1–A4 show typical PDS and fit residuals for HXMT data and NICER data of GX 339-4 and EXO 1846-031, respectively, and the right panels show typical spectra and fit residuals. In Tables A1 and A2, we summarize the selected observations that are analyzed in this work. Tables A3 and A4 show the best-fit results of GX 339-4 and EXO 1846-031, respectively.

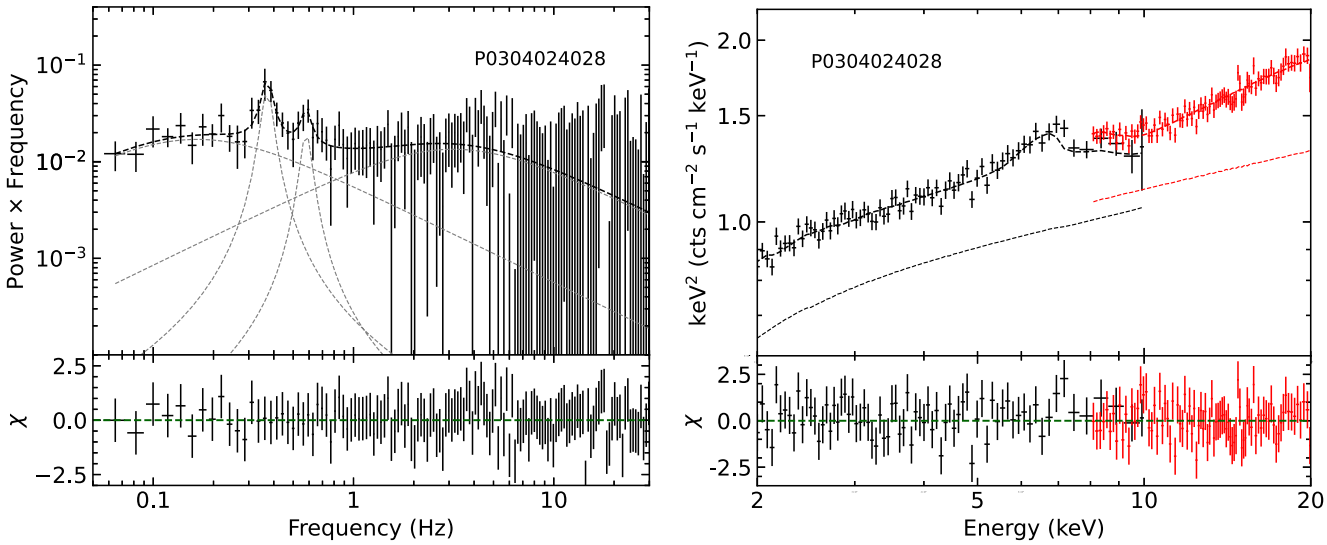

Figure A1. Left: a typical PDS of GX 339−4 from HXMT data (Obs ID: P0304024028). Right: the HXMT spectrum and residuals to the best-fit model for the same observation. Data from the LE and ME detectors are denoted in black and red, respectively.

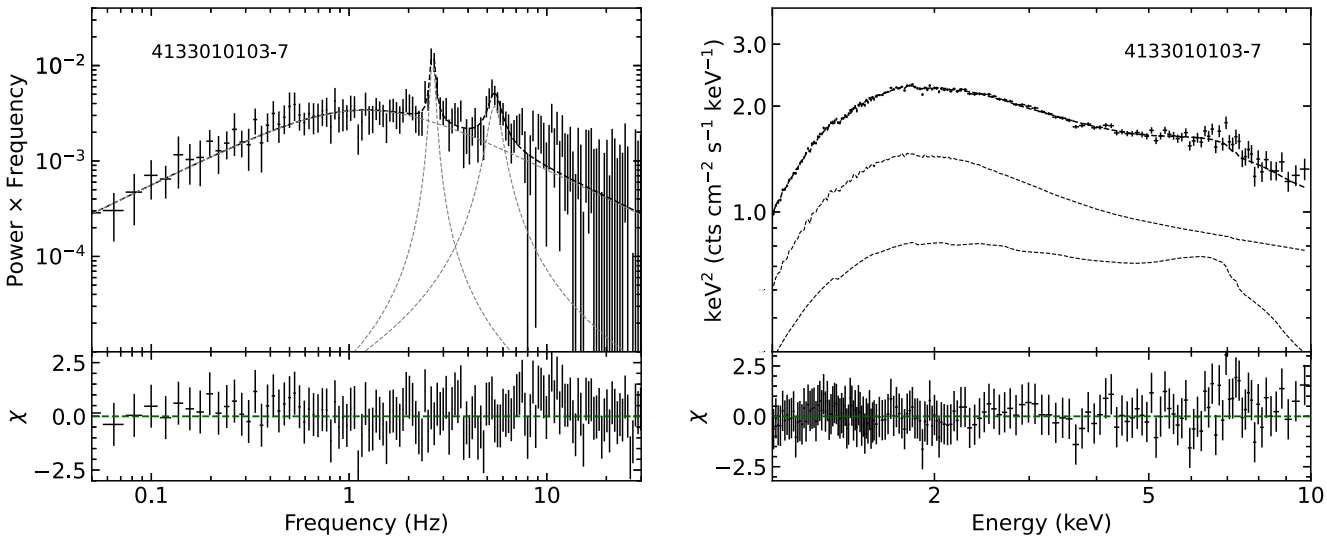

Figure A2. Left: a typical PDS of GX 339−4 from NICER data (Obs ID: 4133010103-7). Right: the NICER spectrum and residuals to the best-fit model for the same observation.

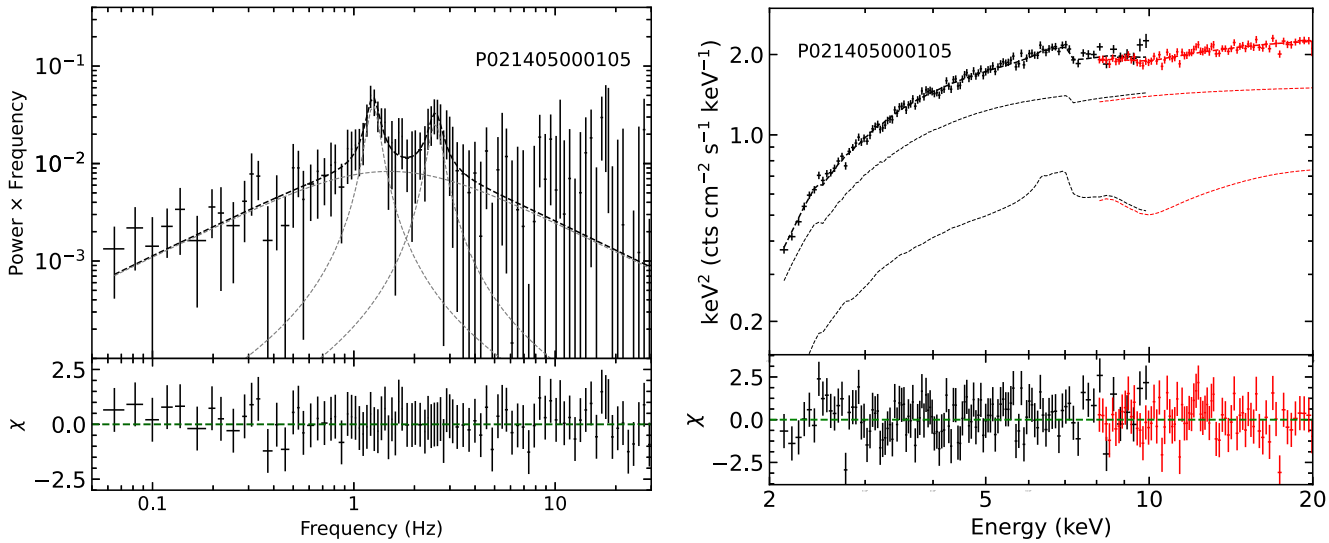

Figure A3. Left: a typical PDS of EXO 1846−031 from HXMT data (Obs ID: P021405000105). Right: the HXMT spectrum and residuals to the best-fit model for the same observation. As in Figure A1, data from the LE and ME detectors are denoted in black and red, respectively.

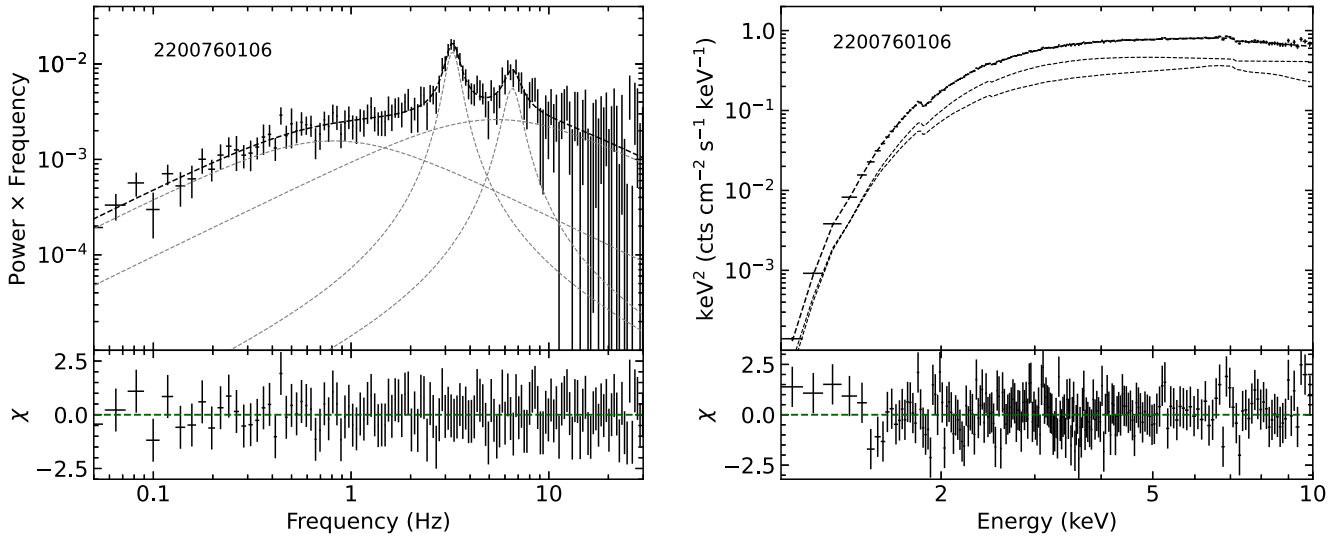

Figure A4. Left: a typical PDS of EXO 1846−031 from NICER data (Obs ID: 2200760106). Right: the NICER spectrum and residuals to the best-fit model for the same observation.

Table A1
HXMT and NICER Observations of GX 339−4 Analyzed in This Work

Mission	Obs. ID	Start Date	Exposure (s)
HXMT	P0304024026	2021-03-12	2274
	P0304024028	2021-03-14	1401
	P0304024032	2021-03-18	1597
	P0304024035	2021-03-22	1669
	P0304024036	2021-03-24	1193
	P0304024038	2021-03-26	2088
NICER	3558011402	2021-03-17	1595
	3558011501	2021-03-19	7560
	4133010101	2021-03-19	2030
	4133010102	2021-03-20	1860
	4133010103	2021-03-26	6111
	4133010104	2021-03-27	8709

Note. For HXMT, the listed exposure time is for the LE instrument.

Table A2
HXMT and NICER Observations of EXO 1846−031 Analyzed in This Work

Mission	Obs. ID	Start Date	Exposure (s)
HXMT	P021405000101	2019-08-02	718
	P021405000102	2019-08-02	1436
	P021405000103	2019-08-02	762
	P021405000104	2019-08-02	718
	P021405000105	2019-08-02	1715
	P021405000106	2019-08-03	563
	P021405000107	2019-08-03	656
	P021405000301	2019-08-05	700
	P021405000302	2019-08-05	1102
	P021405000303	2019-08-05	678
	P021405000401	2019-08-06	718
	P021405000502	2019-08-07	691
	P021405000503	2019-08-07	539
	P021405000601	2019-08-08	1130
	P021405000701	2019-08-08	1163
	P021405000702	2019-08-09	1795
NICER	2200760101	2019-07-31	5658
	2200760102	2019-08-01	1165
	2200760103	2019-08-02	2562
	2200760104	2019-08-03	1488
	2200760105	2019-08-04	1130
	2200760106	2019-08-05	3564
	2200760107	2019-08-06	912
	2200760108	2019-08-07	927
	2200760109	2019-08-08	3293
	2200760110	2019-08-09	4629
	2200760112	2019-08-11	2749
	2200760113	2019-08-12	3341
	2200760114	2019-08-13	7154
	2200760115	2019-08-13	8181
	2200760116	2019-08-15	4703
	2200760117	2019-08-16	8739
	2200760118	2019-08-17	4875
	2200760119	2019-08-17	3341
	2200760120	2019-08-19	3894

Note. As in the case of GX 339−4, the listed exposure time is for the LE instrument of HXMT.

Table A3
Best-fit Parameters of GX 339−4

Obs. ID	$N_{\rm H}$ (10^{22} cm^{-2})	$f_{\rm QPO}$	Γ	$f_{\rm sc}$	$\dot{M}$ (10^{15} g s^{-1})	$R_{\rm in}$ ($R_{\rm g}$)	log$F_{\rm con}$	log$F_{\rm ref}$	χ^2/ν
P0304024026	0.55^{*}	$0.276^{+0.022}_{-0.025}$	$1.748^{+0.022}_{-0.025}$	$0.40^{+P}_{-0.21}$	$0.39^{+1.7}_{-0.13}$	40^{+57}_{-13}	$-8.38^{+0.26}_{-0.25}$	$-8.76^{+0.21}_{-0.25}$	893.93/1057
P0304024028	0.55^{*}	$0.370^{+0.016}_{-0.012}$	$1.788^{+0.023}_{-0.03}$	$0.6^{+0.17}_{-0.4}$	$0.21^{+1.2}_{-0.05}$	22^{+13}_{-6}	$-8.34^{+0.06}_{-0.19}$	$-8.89^{+0.20}_{-0.4}$	833.81/959
P0304024032	0.55^{*}	$0.428^{+0.013}_{-0.019}$	$1.812^{+0.025}_{-0.014}$	$0.44^{+P}_{-0.11}$	$0.8^{+2.9}_{-0.4}$	55.6^{+44}_{-7}	$-8.17^{+0.18}_{-0.3}$	$-8.92^{+0.3}_{-0.18}$	911.31/1013
P0304024035	0.55^{*}	0.66 ± 0.04	$1.851^{+0.028}_{-0.024}$	$0.56^{+0.09}_{-0.11}$	$0.31^{+0.3}_{-0.08}$	$18.2^{+13}_{-2.4}$	$-8.16^{+0.06}_{-0.15}$	$-8.89^{+0.4}_{-0.25}$	930.44/1033
P0304024036	0.55^{*}	0.93 ± 0.05	$1.831^{+0.022}_{-0.04}$	0.50 ± 0.04	0.33 ± 0.05	$15.5^{+3.0}_{-2.7}$	$-8.12^{+0.25}_{-0.3}$	$-8.52^{+0.3}_{-0.24}$	948.06/1021
P0304024038	0.55^{*}	2.53 ± 0.06	$2.338^{+0.021}_{-0.023}$	$0.432^{+0.016}_{-0.017}$	$0.84^{+0.03}_{-0.04}$	$15.4^{+0.6}_{-0.7}$	$-8.01^{+0.3}_{-0.5}$	$-8.61^{+0.23}_{-0.15}$	959.94/977
3558011402	0.62 ± 0.04	0.407 ± 0.019	$1.703^{+0.023}_{-0.024}$	$0.5^{+0.20}_{-0.4}$	$0.35^{+0.20}_{-0.18}$	36.3^{+8}_{-12}	$-8.30^{+0.07}_{-0.7}$	$-8.60^{+0.2}_{-0.11}$	684.37/852
3558011501	0.557 ± 0.004	$0.492^{+0.018}_{-0.015}$	$1.7186^{+0.0022}_{-0.0024}$	$0.69^{+0.11}_{-0.10}$	0.207 ± 0.005	21.7 ± 1.1	-8.303 ± 0.017	-8.67 ± 0.04	587.78/899
4133010101	$0.617^{+0.12}_{-0.025}$	$0.491^{+0.03}_{-0.017}$	$1.711^{+0.02}_{-0.029}$	$0.48^{+0.21}_{-0.22}$	$0.30^{+0.16}_{-0.09}$	31.1^{+10}_{-7}	$-8.38^{+0.06}_{-0.29}$	$-8.48^{+0.11}_{-0.09}$	725.14/889
4133010102	$0.580^{+0.04}_{-0.018}$	$0.520^{+0.026}_{-0.028}$	$1.715^{+0.019}_{-0.024}$	$0.6^{+0.20}_{-0.5}$	$0.23^{+0.04}_{-0.06}$	$23.1^{+4}_{-1.9}$	$-8.32^{+0.06}_{-0.6}$	$-8.61^{+0.16}_{-0.06}$	691.04/886
4133010103-1	$0.457^{+0.018}_{-0.03}$	$1.97^{+0.05}_{-0.06}$	$2.247^{+0.03}_{-0.018}$	$0.517^{+0.005}_{-0.04}$	$0.64^{+0.16}_{-0.11}$	20 ± 3	$-8.27^{+0.09}_{-0.12}$	$-8.67^{+0.20}_{-0.3}$	581.61/709
4133010103-2	$0.487^{+0.021}_{-0.029}$	$1.98^{+0.04}_{-0.06}$	$2.12^{+0.05}_{-0.06}$	$0.32^{+0.11}_{-0.3}$	0.57 ± 0.25	18 ± 5	$-8.27^{+0.15}_{-0.6}$	$-8.28^{+0.22}_{-0.23}$	604.52/719
4133010103-3	0.46 ± 0.03	2.20 ± 0.04	$2.16^{+0.05}_{-0.06}$	$0.43^{+0.07}_{-0.19}$	$0.41^{+0.08}_{-0.11}$	$13.9^{+2.1}_{-2.2}$	$-8.28^{+0.09}_{-0.24}$	$-8.66^{+0.4}_{-0.28}$	594.45/683
4133010103-4	0.489 ± 0.027	$2.54^{+0.05}_{-0.04}$	$2.26^{+0.08}_{-0.07}$	$0.38^{+0.10}_{-0.25}$	$0.39^{+0.07}_{-0.13}$	12 ± 3	$-8.29^{+0.11}_{-0.4}$	$-8.51^{+0.3}_{-0.27}$	609.25/715
4133010103-5	$0.481^{+0.027}_{-0.023}$	$2.69^{+0.04}_{-0.05}$	$2.30^{+0.05}_{-0.12}$	$0.45^{+0.07}_{-0.15}$	$0.46^{+0.11}_{-0.13}$	$12.9^{+2.6}_{-2.7}$	$-8.20^{+0.06}_{-0.14}$	-8.68 ± 0.26	605.14/718
4133010103-6	$0.473^{+0.021}_{-0.018}$	$2.55^{+0.03}_{-0.04}$	$2.20^{+0.06}_{-0.07}$	$0.37^{+0.07}_{-0.13}$	$0.46^{+0.11}_{-0.12}$	12.7 ± 2.5	$-8.21^{+0.06}_{-0.18}$	$-8.49^{+0.22}_{-0.14}$	550.91/763
4133010103-7	$0.488^{+0.023}_{-0.022}$	$2.64^{+0.03}_{-0.02}$	$2.28^{+0.06}_{-0.09}$	$0.39^{+0.08}_{-0.13}$	$0.47^{+0.13}_{-0.11}$	$13.2^{+2.8}_{-2.6}$	$-8.23^{+0.09}_{-0.13}$	$-8.43^{+0.15}_{-0.19}$	641.36/781
4133010103-8	$0.495^{+0.018}_{-0.021}$	$2.91^{+0.03}_{-0.04}$	$2.35^{+0.06}_{-0.08}$	$0.44^{+0.08}_{-0.11}$	$0.51^{+0.13}_{-0.11}$	$12.7^{+2.7}_{-2.4}$	$-8.17^{+0.06}_{-0.11}$	-8.50 ± 0.17	609.30/776
4133010103-9	$0.504^{+0.015}_{-0.02}$	$3.06^{+0.03}_{-0.02}$	$2.35^{+0.06}_{-0.11}$	$0.40^{+0.09}_{-0.14}$	$0.44^{+0.11}_{-0.09}$	$11.0^{+2.2}_{-2.3}$	$-8.23^{+0.08}_{-0.13}$	-8.35 ± 0.13	620.33/788
4133010104-1	$0.500^{+0.020}_{-0.019}$	3.28 ± 0.05	$2.35^{+0.09}_{-0.16}$	$0.37^{+0.16}_{-0.22}$	$0.42^{+0.14}_{-0.13}$	$10.1^{+2.7}_{-2.6}$	$-8.22^{+0.10}_{-0.5}$	$-8.39^{+0.29}_{-0.22}$	645.09/762
4133010104-2	$0.502^{+0.023}_{-0.021}$	$3.20^{+0.03}_{-0.04}$	$2.39^{+0.05}_{-0.09}$	$0.45^{+0.06}_{-0.10}$	$0.51^{+0.08}_{-0.12}$	$11.9^{+1.5}_{-2.5}$	$-8.15^{+0.05}_{-0.11}$	$-8.47^{+0.17}_{-0.14}$	618.63/763
4133010104-3	$0.500^{+0.027}_{-0.029}$	$3.04^{+0.14}_{-0.26}$	$2.46^{+0.07}_{-0.22}$	$0.50^{+0.08}_{-0.29}$	$0.69^{+0.19}_{-0.17}$	$13.2^{+2.8}_{-4}$	$-8.04^{+0.07}_{-0.5}$	$-8.46^{+0.4}_{-0.28}$	547.62/656
4133010104-4	$0.507^{+0.028}_{-0.029}$	$3.04^{+0.14}_{-0.26}$	$2.34^{+0.14}_{-0.22}$	$0.36^{+0.21}_{-P}$	0.6 ± 0.3	12 ± 5	$-8.11^{+0.11}_{-0.5}$	$-8.3^{+0.3}_{-0.8}$	565.97/656
4133010104-5	0.48 ± 0.03	$3.41^{+0.07}_{-0.06}$	$2.4^{+0.10}_{-0.3}$	$0.41^{+0.19}_{-P}$	$0.34^{+0.08}_{-0.17}$	$8.5^{+2.9}_{-2.8}$	$-8.26^{+0.07}_{-0.5}$	$-8.6^{+0.4}_{-0.6}$	502.43/616
4133010104-6	0.50 ± 0.02	3.63 ± 0.06	$2.38^{+0.09}_{-0.12}$	$0.40^{+0.09}_{-0.14}$	$0.50^{+0.12}_{-0.11}$	10.6 ± 2.2	$-8.14^{+0.07}_{-0.12}$	$-8.50^{+0.20}_{-0.21}$	559.10/776
4133010104-7	$0.500^{+0.019}_{-0.022}$	$3.97^{+0.10}_{-0.08}$	$2.39^{+0.11}_{-0.18}$	$0.37^{+0.1}_{-0.17}$	$0.36^{+0.09}_{-0.08}$	$8.2^{+1.8}_{-1.9}$	$-8.23^{+0.07}_{-0.15}$	-8.56 ± 0.22	559.05/700
4133010104-8	$0.534^{+0.03}_{-0.024}$	$3.99^{+0.05}_{-0.06}$	$2.52^{+0.17}_{-0.28}$	$0.40^{+0.23}_{-0.4}$	$0.34^{+0.11}_{-0.14}$	$7.7^{+2.8}_{-2.9}$	$-8.26^{+0.12}_{-0.4}$	$-8.46^{+0.3}_{-0.23}$	515.87/692
4133010104-9	$0.512^{+0.023}_{-0.026}$	$3.99^{+0.05}_{-0.06}$	$2.50^{+0.13}_{-0.19}$	$0.37^{+0.1}_{-0.18}$	$0.34^{+0.07}_{-0.08}$	$7.1^{+1.4}_{-1.3}$	$-8.25^{+0.07}_{-0.14}$	$-8.53^{+0.19}_{-0.20}$	611.50/685
4133010104-10	$0.528^{+0.019}_{-0.018}$	4.55 ± 0.08	$2.57^{+0.11}_{-0.15}$	$0.36^{+0.1}_{-0.13}$	0.48 ± 0.09	$7.4^{+1.5}_{-1.1}$	$-8.10^{+0.05}_{-0.12}$	$-8.44^{+0.19}_{-0.16}$	591.18/774
4133010104-11	$0.500^{+0.022}_{-0.018}$	4.34 ± 0.04	$2.42^{+0.14}_{-0.21}$	$0.30^{+0.12}_{-0.17}$	$0.38^{+0.06}_{-0.07}$	$6.8^{+1.4}_{-1.3}$	$-8.19^{+0.07}_{-0.10}$	$-8.51^{+0.22}_{-0.20}$	544.57/701
4133010104-12	$0.526^{+0.025}_{-0.022}$	4.81 ± 0.07	$2.62^{+0.13}_{-0.20}$	$0.37^{+0.11}_{-0.13}$	$0.42^{+0.08}_{-0.09}$	6.8 ± 1.4	$-8.14^{+0.05}_{-0.14}$	$-8.60^{+0.26}_{-0.18}$	536.68/698
4133010104-13	$0.528^{+0.016}_{-0.024}$	$5.37^{+0.23}_{-0.19}$	$2.70^{+0.14}_{-0.29}$	$0.39^{+0.12}_{-0.20}$	$0.54^{+0.09}_{-0.10}$	7.7 ± 1.7	$-8.06^{+0.04}_{-0.18}$	$-8.67^{+0.4}_{-0.24}$	564.02/718

Note. The symbol * indicates that the parameter is frozen in the fit. log $F_{\rm con}$ and log $F_{\rm ref}$ represent the 1–20 keV flux of the continuum (disk and Comptonization) and reflection components, respectively. The symbol P means that the error bar touches the lower (or higher) limit. All uncertainties are quoted at the 90% confidence level.

Table A4
Best-fit Parameters of EXO 1846−031

Obs. ID	$N_{\rm H}$ (10^{22} cm^{-2})	QPO Frequency	Γ	$f_{\rm sc}$	$\dot{M}$ (10^{15} g s^{-1})	$R_{\rm in}$ ($R_{\rm g}$)	log$F_{\rm con}$	log$F_{\rm ref}$	χ^2/ν
P021405000101	$6.73^{+0.24}_{-0.19}$	$0.689^{+0.011}_{-0.009}$	$1.81^{+0.07}_{-0.04}$	$0.09^{+0.08}_{-0.04}$	$6.0^{+1.1}_{-2.2}$	99^{+P}_{-58}	$-8.04^{+0.11}_{-0.16}$	$-8.74^{+0.5}_{-0.24}$	1016.51/1051
P021405000102	$7.4^{+0.8}_{-0.7}$	$0.851^{+0.011}_{-0.012}$	1.82 ± 0.04	$0.32^{+0.21}_{-0.11}$	$0.9^{+0.9}_{-0.5}$	25^{+20}_{-10}	-8.05 ± 0.09	$-8.75^{+0.5}_{-0.21}$	988.95/1022
P021405000103	$8.7^{+1.5}_{-1.1}$	0.994 ± 0.012	$1.95^{+0.04}_{-0.05}$	$0.13^{+0.05}_{-0.03}$	$5.2^{+2.1}_{-1.8}$	55^{+41}_{-16}	$-7.92^{+0.09}_{-0.18}$	$-8.77^{+0.5}_{-0.28}$	1026.72/1022
P021405000104	$7.6^{+0.6}_{-0.5}$	$1.132^{+0.019}_{-0.021}$	$2.02^{+0.06}_{-0.06}$	$0.17^{+0.16}_{-0.05}$	$6.4^{+2.5}_{-4}$	83^{+17}_{-50}	$-8.08^{+0.09}_{-0.11}$	$-8.50^{+0.08}_{-0.25}$	1030.04/1019
P021405000105	$8.0^{+P}_{-0.5}$	1.251 ± 0.014	$1.964^{+0.05}_{-0.024}$	$0.20^{+0.10}_{-0.03}$	$2.8^{+2.0}_{-1.3}$	41^{+15}_{-12}	$-8.03^{+0.03}_{-0.05}$	-8.5 ± 0.4	1073.18/1139
P021405000106	$6.13^{+0.3}_{-0.17}$	$1.340^{+0.009}_{-0.011}$	$2.029^{+0.06}_{-0.017}$	$0.989^{+P}_{0.021}$	$0.29^{+0.09}_{-0.04}$	$9.94^{+4}_{-0.16}$	$-8.18^{+0.04}_{-0.3}$	$-8.51^{+0.06}_{-0.25}$	994.17/922
P021405000107	$6.59^{+0.27}_{-0.5}$	$1.60^{+0.04}_{-0.05}$	2.05 ± 0.07	$0.51^{+P}_{-0.29}$	$1.0^{+0.9}_{-0.3}$	29^{+20}_{-8}	$-8.03^{+0.15}_{-1.9}$	$-8.8^{+0.8}_{-1.0}$	954.56/967
P021405000201	$6.35^{+0.5}_{-0.23}$	$2.26^{+0.04}_{-0.06}$	$2.245^{+0.05}_{-0.028}$	$0.28^{+0.4}_{-0.08}$	6^{+6}_{-4}	100^{+P}_{-56}	$-8.00^{+0.12}_{-0.6}$	-8.5 ± 0.4	947.89/1006
P021405000301	$5.5^{+0.4}_{-0.5}$	3.14 ± 0.03	$2.41^{+0.09}_{-0.07}$	$0.55^{+0.12}_{-0.06}$	$0.39^{+0.3}_{-0.15}$	$6.0^{+6}_{-2.3}$	$-8.00^{+0.03}_{-0.15}$	$-8.8^{+0.6}_{-0.5}$	1043.07/1056
P021405000302	$6.12^{+0.4}_{-0.26}$	3.18 ± 0.07	2.43 ± 0.07	0.50 ± 0.05	$0.36^{+0.15}_{-0.10}$	$5.5^{+3}_{-1.2}$	$-8.14^{+0.16}_{-0.15}$	$-8.1^{+0.14}_{-0.7}$	1007.96/1113
P021405000303	$6.2^{+1.2}_{-0.7}$	3.73 ± 0.05	$2.11^{+0.18}_{-0.11}$	$0.004^{+0.5}_{-P}$	0.09 ± 0.06	3.5 ± 1.2	$-8.64^{+0.8}_{-0.08}$	$-7.89^{+0.04}_{-0.8}$	889.98/912
P021405000401	5.1 ± 0.6	$3.26^{+0.13}_{-0.11}$	$2.22^{+0.10}_{-0.06}$	$0.47^{+0.09}_{-0.06}$	$0.29^{+0.19}_{-0.09}$	$4.4^{+2.5}_{-1.4}$	$-7.93^{+0.05}_{-0.4}$	$-8.9^{+0.9}_{-1.1}$	835.45/909
P021405000502	$5.6^{+0.3}_{-0.6}$	$4.19^{+0.15}_{-0.13}$	$2.43^{+0.09}_{-0.04}$	$0.420^{+0.018}_{-0.05}$	$0.50^{+0.18}_{-0.17}$	$6.0^{+0.7}_{-1.6}$	$-7.90^{+0.03}_{-0.04}$	$-9.1^{+0.6}_{-0.3}$	993.15/989
P021405000503	$6.4^{+0.7}_{-0.5}$	3.90 ± 0.09	$2.54^{+0.1}_{-0.11}$	$0.35^{+0.04}_{-0.05}$	$0.62^{+0.17}_{-0.24}$	$6.8^{+1.1}_{-2.2}$	$-8.02^{+0.09}_{-0.06}$	$-8.21^{+0.15}_{-0.3}$	937.30/953
P021405000601	$6.01^{+0.27}_{-0.4}$	4.48 ± 0.05	$2.57^{+0.06}_{-0.08}$	$0.403^{+0.027}_{-0.03}$	$0.75^{+0.12}_{-0.19}$	$7.4^{+0.9}_{-1.6}$	$-7.92^{+0.08}_{-0.05}$	$-8.29^{+0.19}_{-0.28}$	1047.54/1021
P021405000701	$6.9^{+0.3}_{-0.5}$	6.69 ± 0.33	$2.44^{+0.05}_{-0.09}$	$0.123^{+0.07}_{--0.067}$	$0.84^{+0.4}_{-0.25}$	$7.1^{+1.0}_{-1.1}$	$-7.98^{+0.26}_{-0.12}$	$-7.83^{+0.10}_{-0.23}$	1059.74/1136
P021405000702	$6.24^{+0.3}_{-0.29}$	$6.31^{+0.14}_{-0.13}$	$2.42^{+0.10}_{-0.06}$	$0.209^{+0.025}_{-0.022}$	$1.16^{+0.14}_{-0.13}$	7.4 ± 0.7	$-7.69^{+0.03}_{-0.21}$	$-9.01^{+0.4}_{-0.18}$	1062.41/1101
2200760101	$6.60^{+0.23}_{-0.24}$	$0.262^{+0.008}_{-0.012}$	$1.609^{+0.017}_{-0.04}$	$0.16^{+0.15}_{-0.06}$	$0.57^{+0.27}_{-0.08}$	33^{+25}_{-14}	$-8.45^{+0.08}_{-0.07}$	$-8.84^{+0.08}_{-0.20}$	799.14/899
2200760102	$7.2^{+0.4}_{-0.3}$	$0.412^{+0.017}_{-0.015}$	$1.81^{+0.11}_{-0.06}$	$0.053^{+0.016}_{-0.007}$	3.1 ± 1.0	90^{+6}_{-28}	$-8.70^{+0.14}_{-0.03}$	-9.0 ± 0.4	704.88/672
2200760103	$6.83^{+0.12}_{-0.2}$	$1.007^{+0.029}_{-0.028}$	$1.972^{+0.04}_{-0.026}$	$0.257^{+0.026}_{-0.04}$	$0.71^{+0.20}_{-0.11}$	33^{+4}_{-3}	$-8.49^{+0.12}_{-0.15}$	$-8.85^{+0.12}_{-0.18}$	861.35/853
2200760104	$6.9^{+0.3}_{-0.4}$	$1.37^{+0.05}_{-0.06}$	$1.877^{+0.027}_{-0.05}$	$0.10^{+0.23}_{-P}$	$0.9^{+0.7}_{-0.6}$	32^{+11}_{-9}	$-8.5^{+0.5}_{-0.3}$	$-8.6^{+0.18}_{-0.03}$	841.57/849
2200760105	$5.66^{+0.11}_{-0.11}$	$2.43^{+0.06}_{-0.06}$	$1.85^{+0.12}_{-0.11}$	$0.39^{+0.05}_{-0.07}$	0.020 ± 0.004	1.9 ± 0.4	$-8.591^{+0.012}_{-0.010}$	$-8.90^{+0.05}_{-0.03}$	728.60/759
2200760106	$5.90^{+0.09}_{-0.08}$	3.25 ± 0.04	$2.15^{+0.16}_{-0.11}$	$0.46^{+0.17}_{-0.13}$	$0.04^{+0.03}_{-0.02}$	$2.8^{+1.2}_{-1.3}$	$-8.61^{+0.16}_{-0.19}$	$-8.76^{+0.19}_{-0.23}$	780.47/863
2200760107	$6.20^{+0.11}_{-0.10}$	3.31 ± 0.05	$2.367^{+0.03}_{-0.028}$	0.6^{*}	$0.07^{+0.07}_{-0.03}$	$4.9^{+2.9}_{-1.6}$	-8.49 ± 0.14	$-8.33^{+0.09}_{-0.15}$	755.51/798
2200760108	$5.99^{+0.17}_{-0.12}$	3.69 ± 0.06	$2.50^{+0.07}_{-0.04}$	0.6^{*}	$0.179^{+0.026}_{-0.07}$	$6.3^{+0.7}_{-1.7}$	$-8.24^{+0.04}_{-0.07}$	$-8.66^{+0.19}_{-0.16}$	709.60/798
2200760109	$6.32^{+0.09}_{-0.11}$	$6.93^{+0.28}_{-0.3}$	$2.20^{+0.18}_{-0.6}$	$0.12^{+0.11}_{-P}$	$0.87^{+0.07}_{-0.11}$	6.3 ± 0.6	$-7.81^{+0.05}_{-0.16}$	$-8.16^{+0.23}_{-0.07}$	755.68/898
2200760110	$6.19^{+0.09}_{-0.04}$	$6.46^{+0.5}_{-0.28}$	$1.80^{+0.6}_{-0.28}$	$0.04^{+0.11}_{-0.04}$	$0.95^{+0.06}_{-0.10}$	$6.3^{+0.6}_{-0.4}$	$-7.81^{+0.06}_{-0.10}$	$-8.15^{+0.14}_{-0.18}$	750.97/899
2200760112	$6.35^{+0.08}_{-0.06}$	$6.16^{+0.5}_{-0.34}$	$2.40^{+0.12}_{-0.23}$	$0.22^{+0.05}_{-0.06}$	$0.86^{+0.08}_{-0.10}$	$7.3^{+0.6}_{-0.4}$	$-7.83^{+0.08}_{-0.05}$	$-8.23^{+0.13}_{-0.06}$	784.13/889
2200760113	$6.56^{+0.11}_{-0.15}$	$6.6^{+1.2}_{-0.5}$	$2.50^{+0.14}_{-0.24}$	$0.17^{+0.07}_{-P}$	$0.12^{+0.04}_{-0.05}$	$3.9^{+0.5}_{-0.7}$	$-8.47^{+0.09}_{-0.21}$	$-8.59^{+0.17}_{-0.23}$	782.20/858
2200760114	$6.28^{+0.15}_{-0.03}$	$5.93^{+0.5}_{-0.20}$	$2.17^{+0.27}_{-0.17}$	$0.08^{+0.11}_{-P}$	$0.40^{+0.06}_{-0.08}$	$5.6^{+0.6}_{-0.5}$	$-8.13^{+0.04}_{-0.14}$	$-8.25^{+0.08}_{-0.3}$	766.57/899
2200760115	$6.35^{+0.11}_{-0.14}$	$5.76^{+0.26}_{-0.23}$	$2.33^{+0.4}_{-0.19}$	$0.12^{+0.25}_{-P}$	$0.13^{+0.04}_{-0.06}$	$4.0^{+1.1}_{-0.5}$	$-8.45^{+0.18}_{-0.14}$	$-8.36^{+0.10}_{-0.10}$	715.46/899
2200760116	$6.19^{+0.12}_{-0.1}$	$5.35^{+0.16}_{-0.18}$	$2.27^{+0.4}_{-0.22}$	$0.18^{+0.3}_{-0.11}$	$0.23^{+0.05}_{-0.06}$	$5.2^{+2.8}_{-0.5}$	$-8.29^{+0.08}_{-0.11}$	$-8.38^{+0.12}_{-0.4}$	812.60/899
2200760117	$6.31^{+0.12}_{-0.14}$	$5.27^{+0.24}_{-0.24}$	$2.25^{+0.5}_{-0.23}$	$0.09^{+0.3}_{-P}$	$0.21^{+0.07}_{-0.06}$	$5.0^{+2.5}_{-0.5}$	$-8.38^{+0.22}_{-0.14}$	$-8.36^{+0.20}_{-0.21}$	723.59/899
2200760118	$6.54^{+0.11}_{-0.09}$	$5.77^{+0.26}_{-0.23}$	$2.81^{+0.11}_{-0.13}$	$0.50^{+0.15}_{-0.10}$	$0.40^{+0.12}_{-0.07}$	$7.8^{+2.4}_{-1.8}$	$-8.14^{+0.05}_{-0.07}$	$-8.49^{+0.06}_{-0.13}$	766.21/899
2200760119	$6.13^{+0.05}_{-0.08}$	$5.18^{+0.15}_{-0.12}$	$2.70^{+0.4}_{-0.18}$	$0.13^{+0.11}_{-0.06}$	$0.281^{+0.04}_{-0.029}$	$4.9^{+0.7}_{-0.4}$	$-8.30^{+0.06}_{-0.07}$	$-8.71^{+0.23}_{-0.18}$	755.06/856
2200760120	$6.41^{+0.26}_{-0.3}$	$5.34^{+0.22}_{-0.15}$	$2.96^{+0.28}_{-0.4}$	$0.22^{+0.14}_{-0.07}$	$0.148^{+0.027}_{-0.029}$	$4.2^{+0.5}_{-0.7}$	$-8.47^{+0.09}_{-0.19}$	$-8.82^{+0.13}_{-0.16}$	736.47/837

Note. This table is organized in the same way as in Table A3. All uncertainties are quoted at the 90% confidence level.

ORCID iDs

Honghui Liu https://orcid.org/0000-0003-2845-1009
Divya Rawat https://orcid.org/0000-0002-9280-2785
Cosimo Bambi https://orcid.org/0000-0002-3180-9502
Ranjeev Misra https://orcid.org/0000-0002-7609-2779
Shuangnan Zhang https://orcid.org/0000-0001-5586-1017

References

Abdikamalov, A. B., Ayzenberg, D., Bambi, C., Liu, H., & Zhang, Y. 2021, PhRvD, 103, 103023
Abramowicz, M., Jaroszynski, M., & Sikora, M. 1978, A&A, 63, 221
Arnaud, K. A. 1996, in ASP Conf. Ser. 101, Astronomical Data Analysis Software and Systems V, ed. G. H. Jacoby & J. Barnes (San Francisco, CA: ASP), 17
Bellavita, C., García, F., Méndez, M., & Karpouzas, K. 2022, MNRAS, 515, 2099
Belloni, T., & Hasinger, G. 1990, A&A, 227, L33
Belloni, T., Klein-Wolt, M., Méndez, M., van der Klis, M., & van Paradijs, J. 2000, A&A, 355, 271
Belloni, T., Psaltis, D., & van der Klis, M. 2002, ApJ, 572, 392
Belloni, T. M. 2010, LNP, 794, 53
Bogensberger, D., Ponti, G., Jin, C., et al. 2020, A&A, 641, A101
Cao, X., Jiang, W., Meng, B., et al. 2020, SCPMA, 63, 249504
Casella, P., Belloni, T., Homan, J., & Stella, L. 2004, A&A, 426, 587
Casella, P., Belloni, T., & Stella, L. 2005, ApJ, 629, 403
Chen, Y., Cui, W., Li, W., et al. 2020, SCPMA, 63, 249505
Done, C., Gierliński, M., & Kubota, A. 2007, A&ARv, 15, 1
Draghis, P. A., Miller, J. M., Cackett, E. M., et al. 2020, ApJ, 900, 78
Dullemond, C. P., & Spruit, H. C. 2005, A&A, 434, 415
Ebisawa, K., Życki, P., Kubota, A., Mizuno, T., & Watarai, K.-y. 2003, ApJ, 597, 780
Fürst, F., Grinberg, V., Tomsick, J. A., et al. 2016, ApJ, 828, 34
Fürst, F., Nowak, M. A., Tomsick, J. A., et al. 2015, ApJ, 808, 122
García, F., Méndez, M., Karpouzas, K., et al. 2021, MNRAS, 501, 3173
García, J., Dauser, T., Lohfink, A., et al. 2014, ApJ, 782, 76
García, J. A., Steiner, J. F., McClintock, J. E., et al. 2015, ApJ, 813, 84
Garg, A., Misra, R., & Sen, S. 2022, MNRAS, 514, 3285
Guo, C.-C., Liao, J.-Y., Zhang, S., et al. 2020, JHEAp, 27, 44
Homan, J., & Belloni, T. 2005, Ap&SS, 300, 107
Huppenkothen, D., Bachetti, M., Stevens, A. L., et al. 2019, ApJ, 881, 39
Ingram, A., & Done, C. 2010, MNRAS, 405, 2447
Ingram, A., Done, C., & Fragile, P. C. 2009, MNRAS, 397, L101
Karpouzas, K., Méndez, M., Ribeiro, E. M., et al. 2020, MNRAS, 492, 1399
Liao, J.-Y., Zhang, S., Chen, Y., et al. 2020b, JHEAp, 27, 24
Liao, J.-Y., Zhang, S., Lu, X.-F., et al. 2020a, JHEAp, 27, 14
Liu, C., Zhang, Y., Li, X., et al. 2020, SCPMA, 63, 249503
Liu, H., Bambi, C., Jiang, J., et al. 2023, ApJ, 950, 5
Liu, H., Ji, L., Bambi, C., et al. 2021a, ApJ, 909, 63
Liu, H., Jiang, J., Zhang, Z., et al. 2022, MNRAS, 513, 4308
Liu, H.-X., Huang, Y., Xiao, G.-C., et al. 2021b, RAA, 21, 070
Ludlam, R. M., Miller, J. M., & Cackett, E. M. 2015, ApJ, 806, 262
Markert, T. H., Canizares, C. R., Clark, G. W., et al. 1973, ApJL, 184, L67
Mastichiadis, A., Petropoulou, M., & Kylafis, N. D. 2022, A&A, 662, A118
Méndez, M., Karpouzas, K., García, F., et al. 2022, NatAs, 6, 577
Miller, J. M., Fabian, A. C., Reynolds, C. S., et al. 2004, ApJL, 606, L131
Misra, R., Rawat, D., Yadav, J. S., & Jain, P. 2020, ApJL, 889, L36
Miyamoto, S., Kitamoto, S., Hayashida, K., & Egoshi, W. 1995, ApJL, 442, L13
Motch, C., Ricketts, M. J., Page, C. G., Ilovaisky, S. A., & Chevalier, C. 1983, A&A, 119, 171
Motta, S., Muñoz-Darias, T., Casella, P., Belloni, T., & Homan, J. 2011, MNRAS, 418, 2292
Negoro, H., Nakajima, M., Sugita, S., et al. 2019, ATel, 12968, 1
Novikov, I. D., & Thorne, K. S. 1973, Black Holes (Les Astres Occlus) (New York: Gordon and Breach), 343
Parker, M. L., Tomsick, J. A., Kennea, J. A., et al. 2016, ApJL, 821, L6
Parmar, A. N., Angelini, L., Roche, P., & White, N. E. 1993, A&A, 279, 179
Peirano, V., Méndez, M., García, F., & Belloni, T. 2023, MNRAS, 519, 1336
Plant, D. S., Fender, R. P., Ponti, G., Muñoz-Darias, T., & Coriat, M. 2014, MNRAS, 442, 1767
Psaltis, D., Belloni, T., & van der Klis, M. 1999, ApJ, 520, 262
Qu, J. L., Lu, F. J., Lu, Y., et al. 2010, ApJ, 710, 836
Rawat, D., Misra, R., Jain, P., & Yadav, J. S. 2022, MNRAS, 511, 1841
Reis, R. C., Fabian, A. C., Ross, R. R., et al. 2008, MNRAS, 387, 1489
Remillard, R. A., Loewenstein, M., Steiner, J. F., et al. 2022, AJ, 163, 130
Rodriguez, J., Varnière, P., Tagger, M., & Durouchoux, P. 2002, A&A, 387, 487
Samimi, J., Share, G. H., Wood, K., et al. 1979, Natur, 278, 434
Shimura, T., & Takahara, F. 1995, ApJ, 445, 780
Sobczak, G. J., Remillard, R. A., Muno, M. P., & McClintock, J. E. 2000, arXiv:astro-ph/0004215
Steiner, J. F., Narayan, R., McClintock, J. E., & Ebisawa, K. 2009, PASP, 121, 1279
Stella, L., & Vietri, M. 1998, ApJL, 492, L59
Titarchuk, L., & Fiorito, R. 2004, ApJ, 612, 988
Titarchuk, L., & Seifina, E. 2009, ApJ, 706, 1463
van der Klis, M. 2005, AN, 326, 798
Varnière, P., Tagger, M., & Rodriguez, J. 2012, A&A, 545, A40
Verner, D. A., Ferland, G. J., Korista, K. T., & Yakovlev, D. G. 1996, ApJ, 465, 487
Vignarca, F., Migliari, S., Belloni, T., Psaltis, D., & van der Klis, M. 2003, A&A, 397, 729
Wang, J., Kara, E., Lucchini, M., et al. 2022, ApJ, 930, 18
Wang, J., Kara, E., Steiner, J. F., et al. 2020, ApJ, 899, 44
Wang-Ji, J., García, J. A., Steiner, J. F., et al. 2018, ApJ, 855, 61
Wijnands, R., Homan, J., & van der Klis, M. 1999, ApJL, 526, L33
Williams, D. R. A., Motta, S. E., Fender, R., et al. 2022, MNRAS, 517, 2801
Wilms, J., Allen, A., & McCray, R. 2000, ApJ, 542, 914
Zdziarski, A. A., Ziółkowski, J., & Mikołajewska, J. 2019, MNRAS, 488, 1026
Zhang, S., Lu, F. J., Zhang, S. N., & Li, T. P. 2014, Proc. SPIE, 9144, 914421
Zhang, S. N., Harmon, B. A., Wilson, C. A., et al. 1994, IAU Circ., 6096, 1
Zhang, S.-N., Li, T., Lu, F., et al. 2020, SCPMA, 63, 249502